CHALMERS

Evaluation of sea level sensors at the Onsala Space Observatory

Master's Thesis in Communication Engineering

JONAS WAHLBOM

Department of Earth and Space Sciences
Chalmers University of Technology
Gothenburg, Sweden 2015

Evaluation of sea level sensors at the Onsala Space Observatory

JONAS WAHLBOM

Department of Earth and Space Sciences
Chalmers University of Technology
SE-412 96 Gothenburg
Sweden
Telephone + 46(0)31-772 1000

Cover: The concrete stilling well with the sea level sensors and the measurement hut at the Onsala Space Observatory.

Evaluation of sea level sensors at the Onsala Space Observatory

JONAS WAHLBOM

Department of Earth and Space Sciences
Chalmers University of Technology
Gothenburg, Sweden 2015

Abstract

A rise of the global mean sea level by more than one metre by the year 2100 is expected. Measurements of the local sea level variations are important to understand the effect on a global scale. This report evaluate a new tide gauge installation at the Onsala Space Observatory with the aim to perform measurements at millimetre accuracy. The new tide gauge consist of two types of level sensors placed in a stilling well. A compact bubbler system and a pulsed radar where the compact bubbler system in the experimental setup consists of a total of five units of which two of the units are of a standard version with a nominal accuracy of 5 mm and three of them of an improved version (called USGS) with a nominal accuracy of 3 mm. Several indoor and field experiments were performed to evaluate the sensors in terms of accuracy, linearity, and stability. A new type of bubble chamber was constructed and compared to the original one. Systematic errors were found when the radar was placed in a narrow tube during the indoor experiments and tendencies of the same systematic error was found in the field experiment even though the tube in this case was significantly wider. A standard deviation of 2.5 mm was found in the differences between the USGS versions in the field environment and a standard deviation of 10 mm between the standard bubbler and the USGS version which was about the same standard deviation that was found between the USGS bubblers and the radar. An improvement was seen in the comparison between the standard bubbler unit and the radar were a standard deviation of 6.5 mm was found. The reason for the better agreement between the less accurate bubbler and the radar is believed to be the timing of the sampling units. The radar and standard bubbler uses the same logging unit and are therefore sampled at the same time. The comparison between the bubbler chambers did not result in any significant differences. This evaluation will serve as a valuable foundation to continued measurements and improvements of the new tide gauge.

keywords: tide gauge, sea level, compact bubbler system, radar

Acknowledgements

First of all I am very thankful to my supervisor Gunnar Elgered for his untiring patience and for providing the necessary guidance throughout the work with this thesis. I would also like to thank the staff at the Onsala Space Observatory for a pleasant work environment and for the fruitful discussions. A special thanks go to Lars Pettersson for his help and useful discussions of all the technical issues and Roger Hammargren for his help with all the practical problems.
I would also like to show my gratitude to the staff at the workshop for all their help, especially Lars Wennerbäck that with his ingenuity solved all practical issues wherever the need arose.

Jonas Wahlbom, 2015

Contents

Chapter 1

Introduction

Continued greenhouse gas emissions during the latest century have an irreversible effect on global warming and a rise of the global mean sea level by more than one metre by the year 2100 is now an accepted possibility, [Overpeck et al., 2012] and [Solomon et al., 2009]. The mean sea water temperature rise which contributes to the sea level rise by thermal expansion of the sea water. Moreover the global warming cause the Greenland and Antarctic ice sheets to melt and transform their land based mass to water. Several attempts to make accurate projections of the local impact of the global rise of the sea level have been made. In [Strauss et al., 2012] high resolution topographic data is used together with local tidal data and population data to model high risk areas along the US coastline. [Vellinga et al., 2012] discuss a worst case climate scenarios impact on the Dutch flood protection are investigated. Information about the local sea level changes is of great importance in both of these examples and as the models get better and better the need for accurate measurements of the local sea level increase.

1.1 Measuring the sea level

The measured sea level can be defined as the sum of the mean sea level, the tide and the meteorological residuals [Manual on Sea-level Measurements and Interpretation , 2006]. The mean sea level can normally be determined by using time series of over a year or longer and average out the more frequent variations such as tides. Tides can be divided into gravitational tide variations caused by the periodic change in the gravitational field from the moon and sun and meteorological tides, caused by periodic changes in atmospheric pressure and winds. Meteorological residuals are irregular events caused by e.g changes in weather and are what is left after the tides are removed. Moreover the sensors used to measure the sea level are in most cases fastened to the land mass and what is actually measured is the difference between the sea level and land. The postglacial land uplift, [Vest, 2006], which can be up to a centimetre per year in Scandinavia on an absolute scale, will therefore also affect the measured sea level.

The accuracy of the techniques based on measuring the pressure depend on the ability to determine the atmospheric pressure as well as the density of the sea water. The sea water density

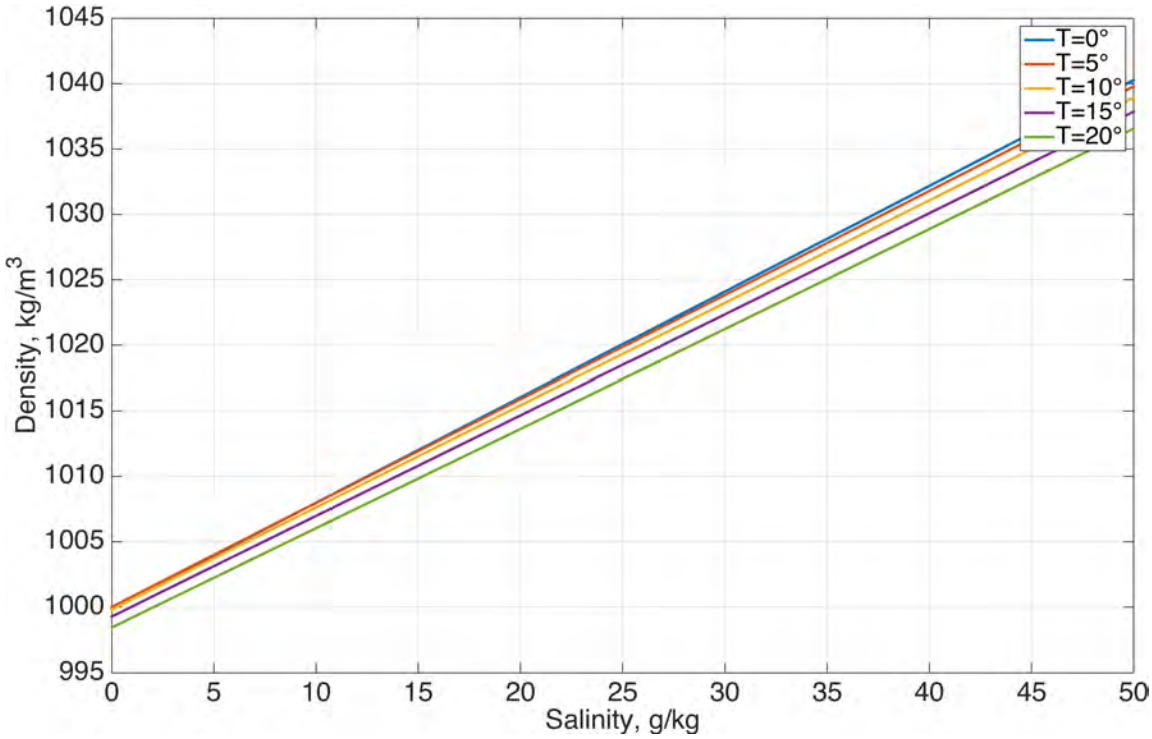

Figure 1.1: The density as a function of salinity at different temperatures.

depend on the water temperature and the salinity according to Figure 1.1. [McCutcheon, S.C. et al. , 1993]. If a radar based technique is used the temperature in the air between the transmitted pulse and the reflecting medium will be a source of error. Moreover, the absolute position of the sensors, and other instrument specific errors such as temperature and aging affect the measurement error.

1.2 Sea level sensors and tide gauges

There are available time series from the English channel from the beginning of the 19th century and well documented time series from 1880 forward from several places around the globe. [Douglas, B. 1991]. There are a number of instruments existing to measure the local sea level change [Manual on Sea-level Measurements and Interpretation , 2006]. Traditionally, stilling wells equipped with a float gauge and a chart recorder or shaft encoder have been used. In the latest decades new technologies emerge such as pneumatic pressure sensors and radars which meet the new demands on accuracy and precision. Often a combination of these are used to construct a reliable and accurate tide gauge. In the latest years GNSS based technologies have also been evaluated [Löfgren , 2014].

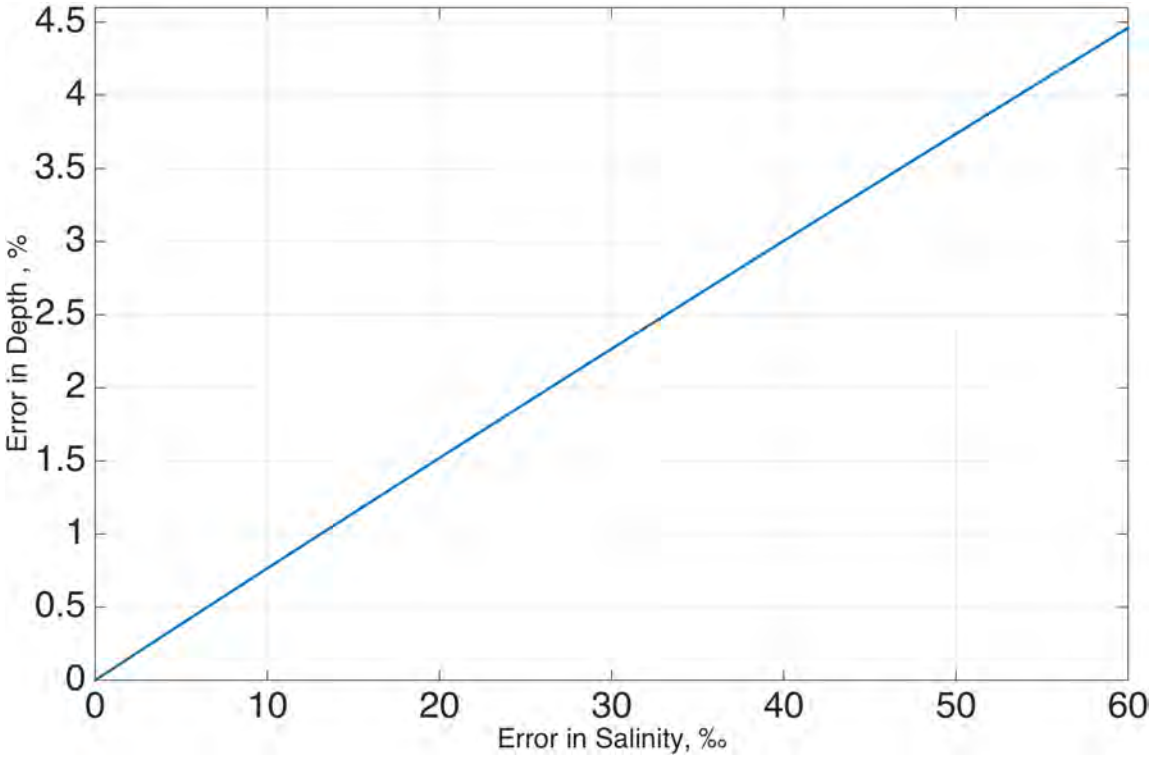

Figure 1.2: The error in calculated depth as a function of the error in salinity at a water temperature of 10 °C.

1.3 Existing sensors at the Onsala Space Observatory

At the Onsala Space Observatory we have the opportunity to connect the local sea level measurements with the geodetic reference frame. Up to now two ways of measuring the local sea level exist at the observatory.

- GNSS (Global Navigation Satellite System). [Löfgren , 2014]
- Pressure gauges. Appendix A

1.3.1 GNSS

As described by [Löfgren , 2014] on estimating the sea level using the GNSS signals reflected off the sea surface:

"*These signals were recorded in two different ways using a GNSS tide gauge at the Onsala Space Observatory, consisting of standard geodetic-type commercially off-the-shelf GNSS equipment. First, the phase-delay of the reflected GNSS signals were recorded directly with a receiver connected to a nadir-looking antenna. Together with the phase-delay of the direct signals, recorded with a receiver connected to a zenith-looking antenna, standard geodetic analysis provided GNSS sea level observations. Second, the Signal-to-Noise Ratio (SNR) recorded with the receiver connected to the zenith- looking antenna, provided an indirect measurement of the reflected GNSS signals, as the reflected signals interfered with the direct GNSS signals and affected the recorded observables. From analysis of the multipath oscillations, an additional type of sea level observation was possible. Furthermore, the SNR-analysis method allowed other GNSS stations, located close to the ocean, in different parts of the world to become GNSS tide gauges.*"

Figure 1.3: The GNSS mareograph at Onsala

1.3.2 Pressure tide gauge

The gauge consist of three pressure sensors mounted in a circle and enclosed in a metallic cylinder fastened to the rock wall. They operate with a 4–20 mA current loop and are sampled with a frequency of 1 Hz using an ADAM unit (Appendix D). They are of differential pressure type and the atmospheric pressure is delivered through an air tube from the shore down to the sensor housing. The pressure sensors were installed in August 2011 and have been operating since then. (Figure 1.4). However, they where damaged by drift ice in the winter 2014 (Figure 1.5) and unpredicted systematic events have been observed. A new more accurate system is therefore needed.

Figure 1.4: The Pressure sensor at Onsala

Figure 1.5: Drift ice damaging the pressure sensor casing.

1.4 New sensors to be evaluated

With the aim to determine the local sea level with an accuracy down to the millimetre level two new instruments are taken into use at the Onsala Space Observatory.

- A bubble sensor, CS471, Compact bubbler system. Appendix B
- A pulsed radar, CS476, Radar Water Level Sensor. Appendix C

This report aim to gain knowledge about their characteristics before the final installation as well as to investigate the measurement uncertainties and linearity at the final site of installation. Chapter 2 describes the hardware and Chapter 3 gives the relevant background theories. The experiments are divided into two parts where the first part, Chapter 4, deals with experiments done mostly in the surroundings of the office building at the observatory and the second part, Chapter 5, is devoted to field experiments done at the site of the final installation.

Chapter 2

Experiment hardware

The two new system types to be installed are described in the following section. In the laboratory experiments a less accurate bubbler unit was used, in the report referred to as $Bubbler_{standard}$. In the field experiments three additional units of a more accurate type were installed alongside the normal unit. The new units are referred to as $Bubbler_{usgs1}$, $Bubbler_{usgs2}$ and $Bubbler_{usgs3}$. There also exist a bubble unit which operates since a year back about 10 meters from the new installation. This unit is of the standard type and will be referred to as $Bubbler_{outside}$.

2.1 The bubbler sensors

The bubbler units are originally manufactured by OTT in Germany and are sold by British Campbell Scientific. To distinguish the normal and the more accurate USGS (U.S. Geological Survey) bubbler unit there is a marking on one of the casing sides. The bubbler system consists of a base unit, Figure 2.1, a plastic air tube and a nozzle. The base unit build up a pressure in the air hose which is submerged in the sea. When the pressure exceed the atmospheric pressure plus the pressure of the column of water above the nozzle outlet, the air will be released from the air hose into the water. By measuring at which pressure this happens at the same time as measuring the atmospheric pressure, the column of water above the outlet can be determined.
The unit communicates through a SDI-12 interface (V.1.3 @1200 baud). Or via a $4-20$ mA current loop (analog signal). In the current setup the SDI 12 interface is used in all cases except for the bubble sensor outside the well used in the field experiments. The bubbler operates at one sample every minute. Technical data for the unit is summarised in Table 2.1.

The air tube can be up to 50 feet (15 m) long and should have a constant negative drop from the unit to the outlet to prevent water from getting into the air hose and to prevent air from gather and condense in the air hose. The bubbler sensors measure the pressure at a specific depth. The pressure depend on the density of the water which is a function of temperature and salinity. At the time of the measurements in this report the salinity levels were unknown and the depth calculated as if we were measuring in freshwater. A corrected value of the depth can be calculated from the old measurements as soon as the salinity is known.

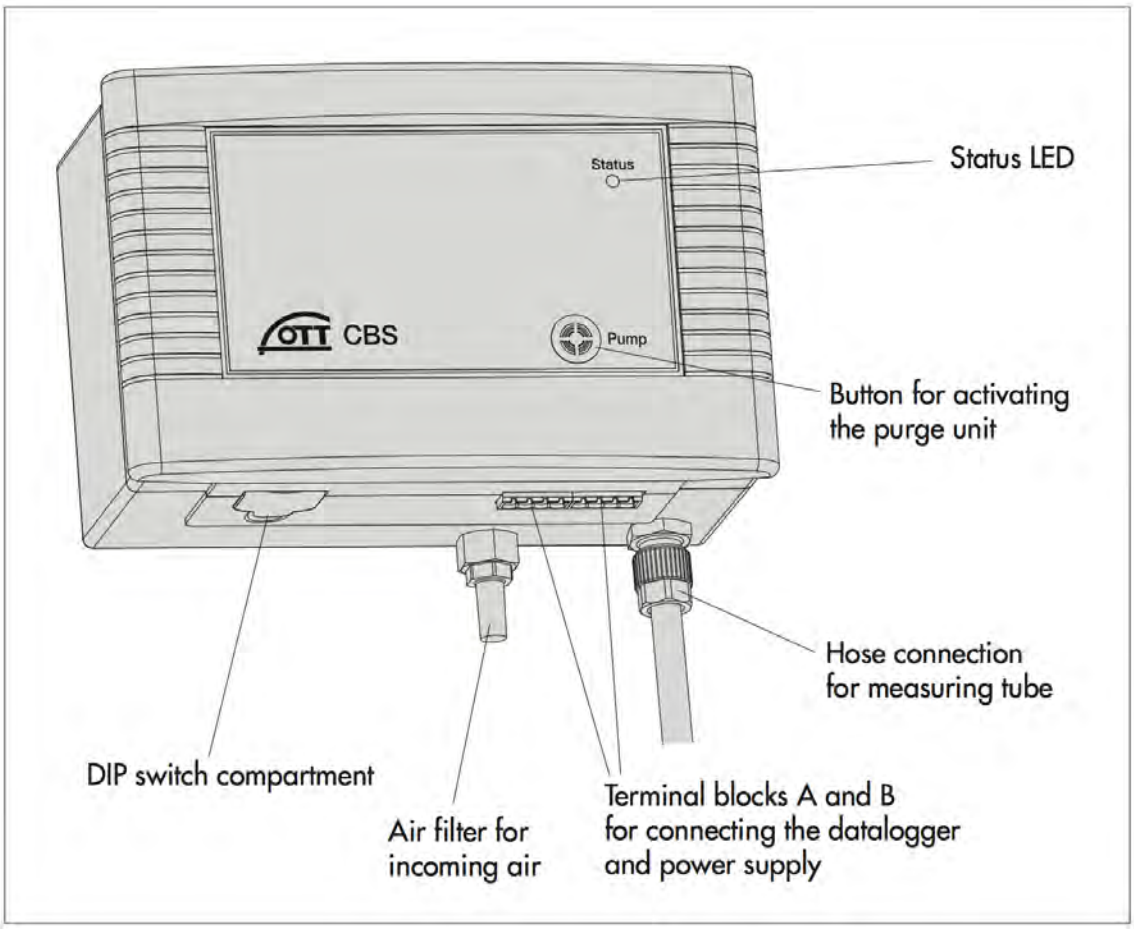

Figure 2.1: The bubbler unit.

2.2 The radar sensor

The radar unit is manufactured by Campbell scientific and communicates through a SDI-12 interface (V.1.3 @1200 baud). Or via a $4-20$ mA current loop (analog signal). In the current setup the SDI 12 interface was used. The radar unit operates at one sample every second. Technical data for the unit is summarised in table 2.1 and the measures of the radar can be seen in Figure 2.2.

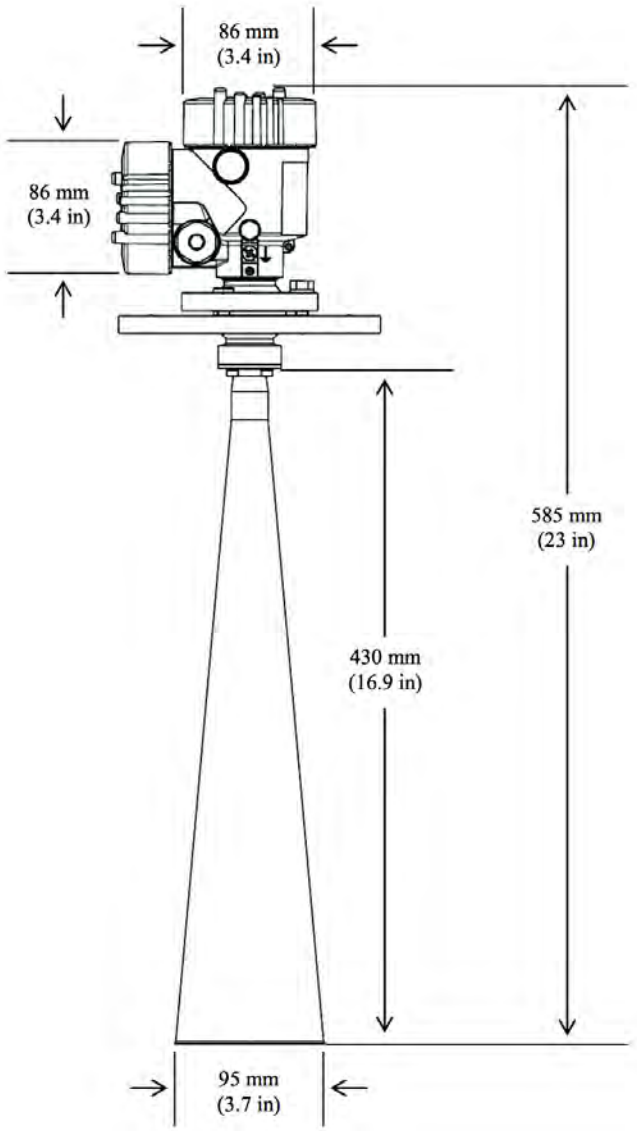

Figure 2.2: The measures of the radar unit.

2.3 The CR1000 datalogger

The radar and the bubble units are sampled with the CR1000 datalogger from Campbel Scientific, see Figure 2.3 and Appendix E. The unit is programmable (CR basic) and can be controlled via an ethernet extension. There are 16 analog inputs and 4 digital ports to be used with e.g the SDI-12 interface. The unit has an internal battery with a lifetime of about 3 years.

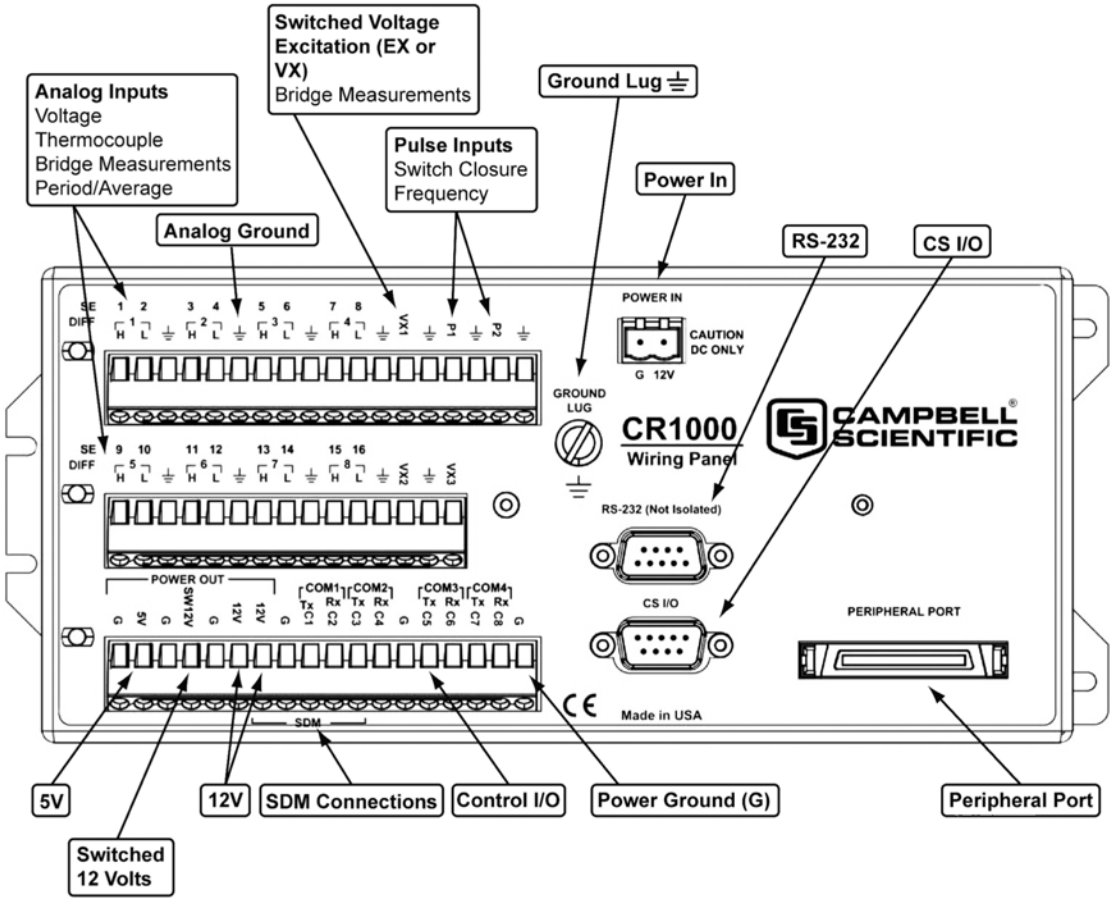

Figure 2.3: The CR1000 unit wiring panel.

Table 2.1: Technical data for the bubble and radar unit

	Bubbler	**Radar**
Power consumption*	typ. 320 mAh/day @ Ts=1 min typ. 25 mAh/day @ Ts=15 min	Sleep: 4.7 mA Meas. 14 mA
Weight	1500 g	-
Temp range	-20 – 60 °C	-40 – 80 °C
Temp sensitivity	-	2 mm/10 K, max 5 mm over the entire temp. range
Relative humidity	operational: 10 – 95 % non condensing	storage: 20–80 %
Dimensions L x W x H	165 mm x 205 mm x 115 mm	150 mm x 150 mm x $(160_{housing} + 430_{horn})$ mm
Tube dimensions	Internal 2 mm, External 4 mm, length max 100 m)	-
Measuring dynamics	1 m/min	-
Accuracy standard unit	0 – 4.57 m ±5 mm 4.57 m - 15 m ±0.065 % of value or ± 6 mm	±3 mm
Accuracy USGS unit	0 – 4.57 m ±3 mm 4.57 m - 15 m ±0.065 % of value or ± 3 mm	-
Resolution	1 mm	1 mm
Pointing sensitivity	-	$\leq$ 1 mm@ ± 2 deg
Range	50 mm – 15 m	50 mm–30 m

*at a supply voltage of 12 V.

Chapter 3

Theory

The output from the experiments are always a time series with one column of unix time stamps and the other with the data. A couple of concepts are needed to investigate these time series and they are presented in the following section.

3.1 Repeatability of acquired time series

A number of measurements $m_1, m_2, ...m_N$ will be separated in time by δt seconds. The repeatability in this report is defined by the standard deviation

$$\sigma = \sqrt{\frac{1}{N-1}\sum_{i=1}^{N}(m_i - \widehat{m})} \tag{3.1}$$

where $\widehat{m}$ is the sample mean of this group of N measurements spread in time by $N \times \delta t$ seconds.

3.2 Linearity in the dynamic range

The linearity of a set of measurements $\mathbf{M} = \mathbf{m_i}, \mathbf{m_{i+1}}, ...\mathbf{m_N}$ can be defined as the ratio of the distance of the sample with the longest perpendicular distance to the polynomial Px estimated to be the best fit in the least-squares sens **and** the measurement range.

$$lin_{\%} = \frac{\max\left(\mathbf{M} - \mathbf{P_x}\right)}{M_{range}} \tag{3.2}$$

where in the case of a linear least square fit

$$P_x = a_1 x + a_0 \tag{3.3}$$

and

$$M_{range} = \max\left(\mathbf{M}\right) - \min\left(\mathbf{M}\right) \tag{3.4}$$

3.3 The position of the water surface in a tank with a bottom outlet

Some of the measurements in this report involve the draining of a water tank. Since we are measuring the distance to the water surface in the tank we need to know the expected position of the surface at a specific time. A tube with a radius r filled with water to a height $h(t)$ contain the water volume $V(t) = h(t)\pi r^2$ at time t. The change of volume per time unit is then

$$\frac{dV}{dt}^{tank} = h'(t)\pi r^2 \tag{3.5}$$

The rate at which water flow out of the outlet at the bottom of the tank depend on the level of water above the outlet and the radius of that outlet. Torricellis law state that the rate at which the water flow out of an outlet at height h below the water surface is proportional to the square root of the height h.

$$\frac{dV}{dt}^{outlet} = -k\sqrt{(h(t))} \tag{3.6}$$

where the constant k depend on the outlet radius and forces such as friction in the outlet tube. However, friction forces are assumed to be of negligible influence in our case and k can be defined as

$$k = \pi a^2\sqrt{2g} \tag{3.7}$$

where a is the radius of the outlet and g is the gravitational acceleration at a given coordinate. Combining Equations (3.5) and (3.6) gives

$$\begin{aligned} \frac{dV}{dt}^{tank} &= \frac{dV}{dt}^{outlet} \\ h'(t)\pi r^2 &= -k\sqrt{(h(t))} \\ h'(t) &= \frac{-k}{\pi r^2}\sqrt{(h(t))} \end{aligned} \tag{3.8}$$

which is a separable first order differential equation. Separating variables and integrating result in

$$\begin{aligned} \frac{1}{\sqrt{(h(t))}}dh &= \frac{-k}{\pi r^2}dt \\ \int \frac{1}{\sqrt{(h(t))}}dh &= \int \frac{-k}{\pi r^2}dt \\ 2\sqrt{(h(t))} &= \frac{-k}{\pi r^2}t + C \end{aligned} \tag{3.9}$$

and we end up with the equation for the height of the water surface at time t

$$h(t) = \left(\frac{\frac{-kt}{\pi r^2} - C}{2}\right)^2 \tag{3.10}$$

where C can be determined by letting $t = 0$

$$\begin{aligned} h(0) &= \left(\frac{-C}{2}\right)^2 \\ C &= -2\sqrt{h(0)} \end{aligned} \tag{3.11}$$

Finally we end up with

$$h(t) = \left(\sqrt{h(0)} - \frac{a^2\sqrt{2g}}{2r^2}t\right)^2 \tag{3.12}$$

where a is the radius of the outlet. An example of Equation (3.12) can be seen in Figure 3.1.

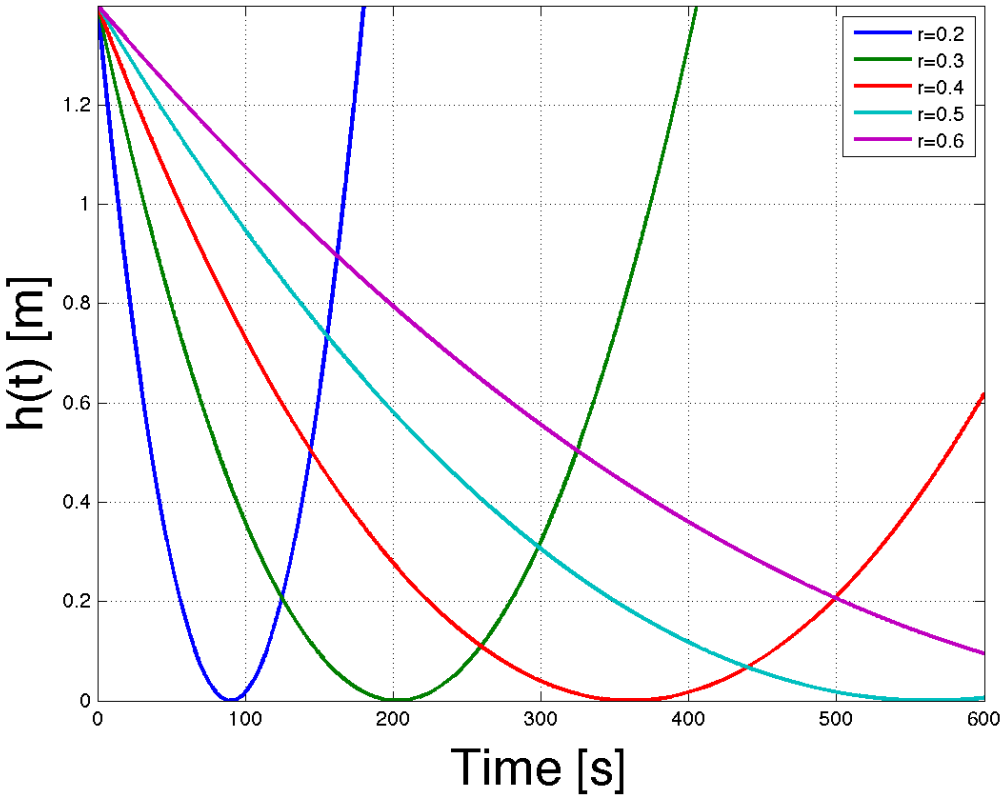

Figure 3.1: The height of the water surface $h(t)$ for 5 different radii of the tube. The equation is only valid for draining of the tank so the solutions beyond h=0 with an increasing h with time shall be neglected.

3.4 Evaporation from a water surface

Some of the measurements span over a relative long period of time and are therefore affected by evaporation. As the water molecules start to evaporated they will saturate the air layer closest to the water surface. The speed at which they evaporate will mostly depend on the difference between the water vapour pressure at the surface layer and that of the ambient air. According to Uno, Paul [1998] the saturation vapor pressure can be determined by

$$e_s = 0.61 \exp\left(\frac{17.3T}{237.3 + T}\right) \tag{3.13}$$

where e_s is the saturated vapour pressure in hPa and T the temperature in Centigrade.

The evaporation rate can then be calculated as

$$E = 0.313(e_s^{water} - re_s^{air})(0.253 + 0.06 \cdot v) \tag{3.14}$$

where

E is the evaporation rate in $kg/m^2 \cdot h$.

e_s^{water} the saturated vapour pressure of the water in hPa.

e_s^{air} the saturated vapour pressure of the air in hPa.

r is the relative humidity of the air.

v the velocity of the wind in m/s.

If we have two level measurements l_1 and l_2 of the water surface level in m and separated in time by dt we can get the right unit by first calculating the weight of the water within those two levels and divide by the area of the surface to get in kg/m^2.

$$\begin{aligned} Water_{weight} &= \frac{(l_1 - l_2) \cdot A \cdot \rho^{water}}{A} \\ &= (l_1 - l_2) \cdot \rho^{water} \end{aligned} \tag{3.15}$$

where A is the area of the surface and ρ^{water} the density of water. Now to get the unit per hour we only need to divide with dt converted to hours. E.g when dt is given in minutes the result looks like

$$E = \frac{(l_1 - l_2) \cdot \rho^{water}}{dt \cdot 60} \tag{3.16}$$

3.5 Measuring range with a pulsed radar

A pulsed radar transmits short pulses of electromagnetic energy which are reflected by the target. If the time between a pulse is transmitted until the same pulse is received is t_{travel} the distance between the reflecting target can be determined by

$$R = \frac{t_{travel} \cdot c}{2} \tag{3.17}$$

where c is the speed of the electromagnetic radiation.
In this report we will investigate a radar situated approximately 4 m above the water surface thus t_{travel} will be about 6.6 ns at 1 m to 33 ns at 5 m (see Figure 3.2). The speed c at which the radio waves travel is affected by the refractive index n of the medium in which they travel.

$$c = \frac{c_o}{n} \tag{3.18}$$

where

$$n = 1 + N \cdot 10^{-6} \tag{3.19}$$

and where N is the refractivity consisting of a dry and a wet term

$$\begin{aligned} N &= N_{dry} + N_{wet} \\ &= 77.6 \cdot \frac{P}{T} + 3.732 \cdot 10^5 \frac{e}{T^2} \end{aligned} \tag{3.20}$$

where:

P: atmospheric pressure (hPa)
e: water vapour pressure (hPa)
T: absolute temperature (K)

The vapour pressure e is related to the relative humidity and saturated vapour pressure according to

$$e = \frac{H \cdot e_s}{100} \tag{3.21}$$

The atmospheric pressure at Onsala vary from about 930 hPa to 1050 hPa. And the temperature from 273 K to 313 K . If these two extreme value are used to calculate a worst case scenario, the deviation in the measured distance due to changes in the refractivity index is 0.1 mm which is much smaller than the nominal accuracy of the radar (3 mm).

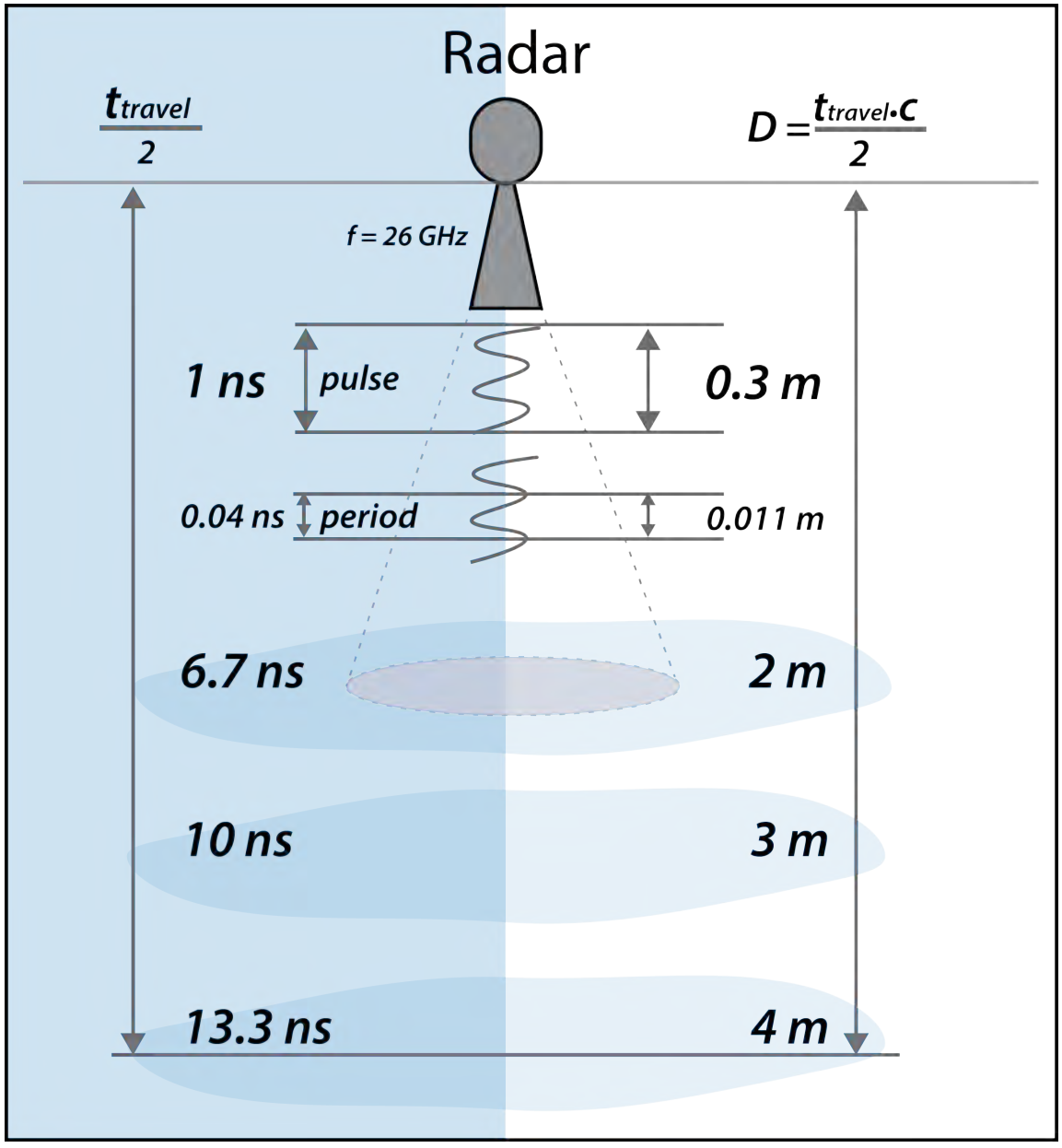

Figure 3.2: A schematic view of the travel time and travel distance of a radar pulse in the well.

3.6 Van der Casteele test

To characterise the systematic errors in the measurements a Van de Casteele test can be performed. By plotting the time series of the measured level H from a reference sensor against the error, $\Delta H = H - H'$, where H' is the level measured by the sensor we want to characterise. If the error is plotted on the x-axis and the reference sensor on the y-axis a perfect sensor would be shown as a vertical line centered at zero which mean the error is the same, in this case zero, regardless on which level we measure. Several types of systematic errors can be characterised by looking at the plots. Figure 3.3 show an example of a scale error using simulated data where one of the sensors measure on a different scale than the other which result in a clear linear slope in the diagram. This is typically the result of an over or under estimation of the water density when using a pressure sensor. Figure 3.5 show the Van de Casteele diagram of the data in Figure 3.4. In this case there is a 15 degrees phase lag introduced in the data, often as a result of a timing error between the sensors.

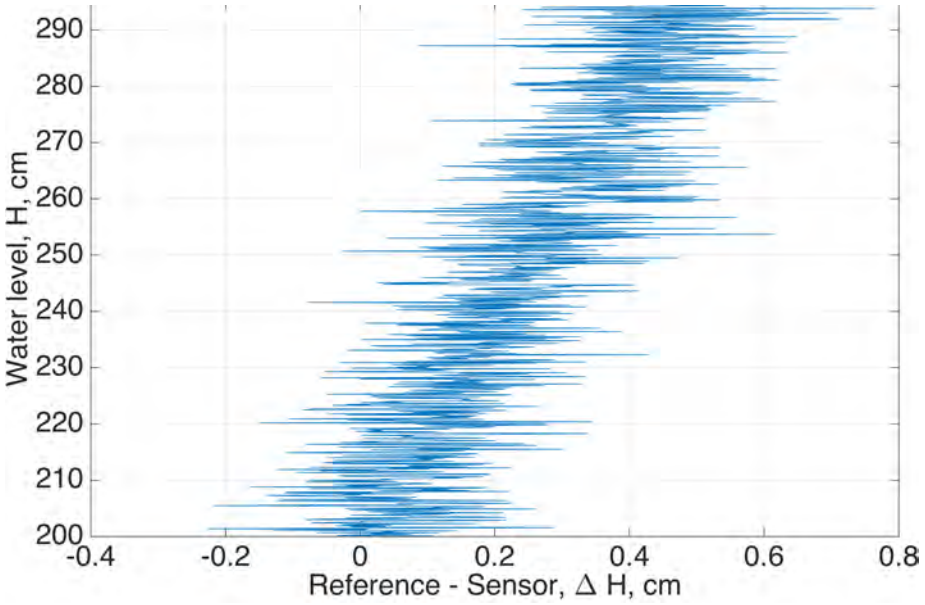

Figure 3.3: The measured water level as a function of the difference between the reference and the sensor we want to characterise.

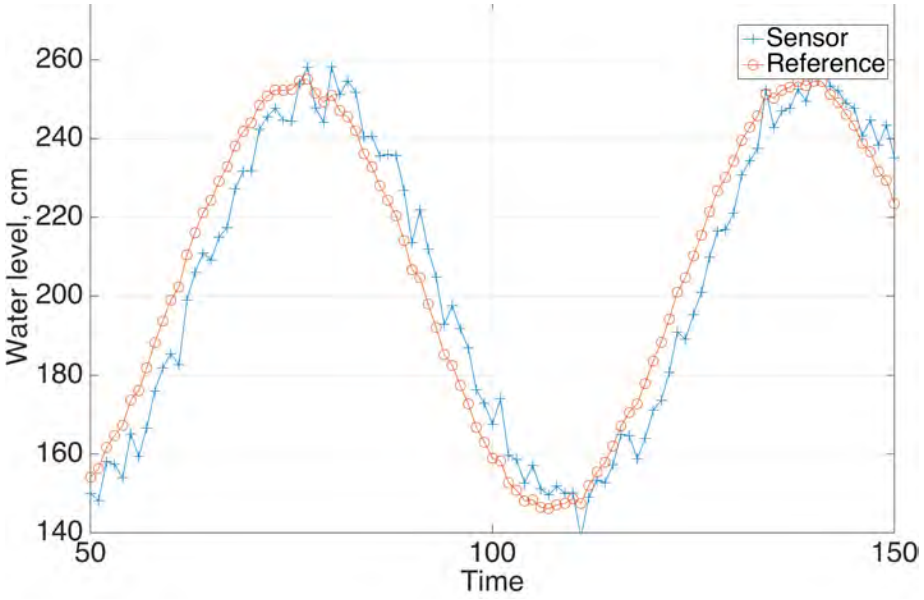

Figure 3.4: Sensor and reference with a phase lag of 15 degrees.

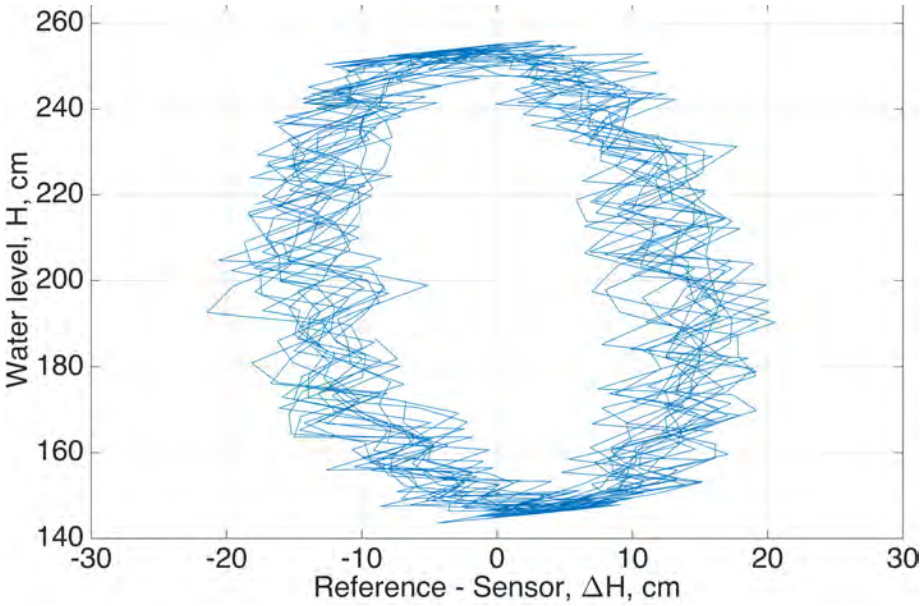

Figure 3.5: The Van de Casteele diagram of the data in Figure 3.4 .

Chapter 4

Laboratory experiments and results

The first part of the experiments took place mainly inside a shower in the office building connected to the 20 m telescope at the observatory and in a pool just outside the office building. In the early months, Mars to June, both the radar and bubbler gauge were left untouched in their tubes which resulted in a series of data were they both tracked the slowly sinking water surface due to evaporation. This resulted in the discovery of a sine formed signal overlaying the radar data, probably due to reflections in the water tank used for the experiments. In the following sections the experiments and the results are presented for each of the gauges starting with the bubble sensor.

4.1 The bubble sensor

The indoor experiments with the bubbler sensor came to an abrupt end when the bubbler sensor possible failed during a measurement. However, the measurements made before the failure are presented in the following section. It should be mentioned that a second bubbler tide gauge have been operating at the observatory site for nearly a year without any problems.

4.1.1 Experiment setup

In the current setup the Bubbler air hose is placed at the bottom of a 150 cm high plexi-glass tube with a diameter of 12 cm. (Figure 4.1). The air hose is held in place by an aluminium rod at the bottom of the tube seen in Figure 4.2. The bubbler and logging units can be seen in Figure 4.3.

4.1.2 A 30 day measurement

A 30 days long measurement was made from the 16th of April to the 16th of May 2014. (Day of year: 106 to 136). The data can be seen in Figure 4.4. Two clear trends due to evaporation are present in the data. One from the 23th of April to the 6th of May, $W_a = -8.37 \cdot 10^{-5}x + m_1$ cm/minute. Another from the 6th of May to the 18th of May $W_b = -6.12 \cdot 10^{-5}x + m_2$ cm/minute. The temperature, pressure and relative humidity during the measurement are plotted in Figure 4.5 and Figure 4.6. The change in the relative humidity coincide with the change of rate of the evaporation and further investigation will show that this surely is the reason.

Figure 4.1: The bubbler air hose placed in a plexi glas tube. The red tube used for the radar measurement can be seen to the right.

Figure 4.2: Air bubbles released from the air hose at the bottom of the tube during a measurement.

Figure 4.3: The green bubbler unit with the surrounding electronics

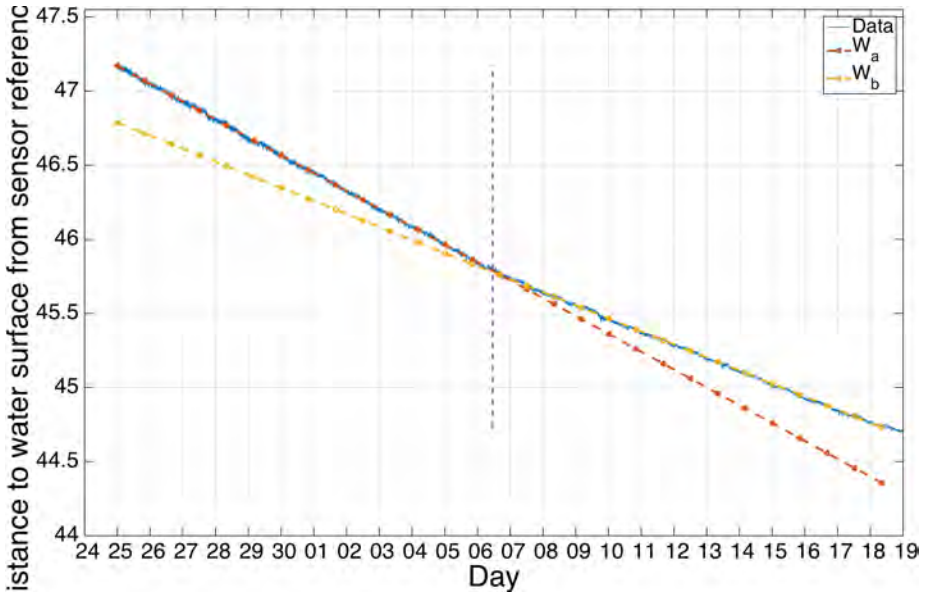

Figure 4.4: 30 days of data plotted together with the linear trend. A change in the rate of evaporation is marked with a vertical dotted line.

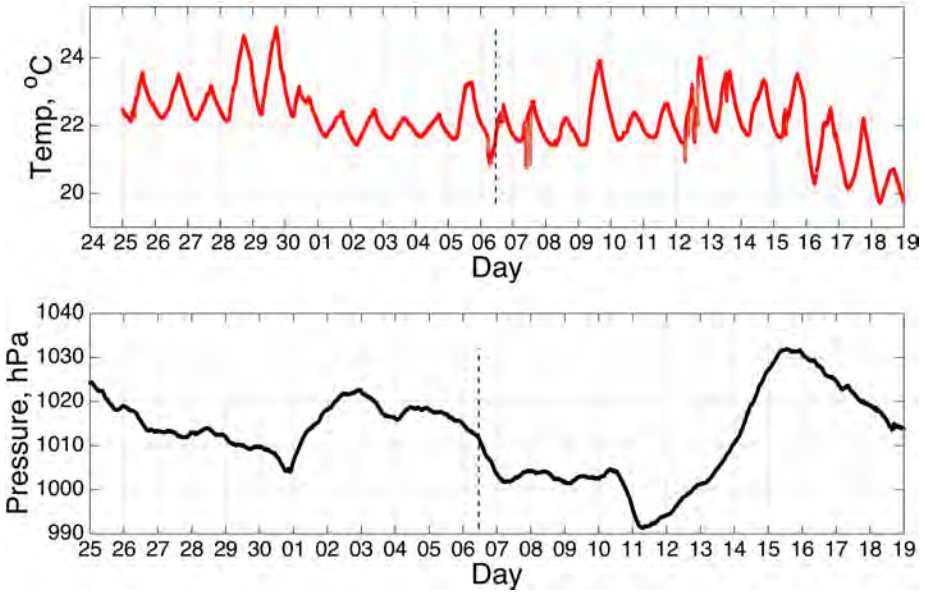

Figure 4.5: Temperature and pressure during the measurement

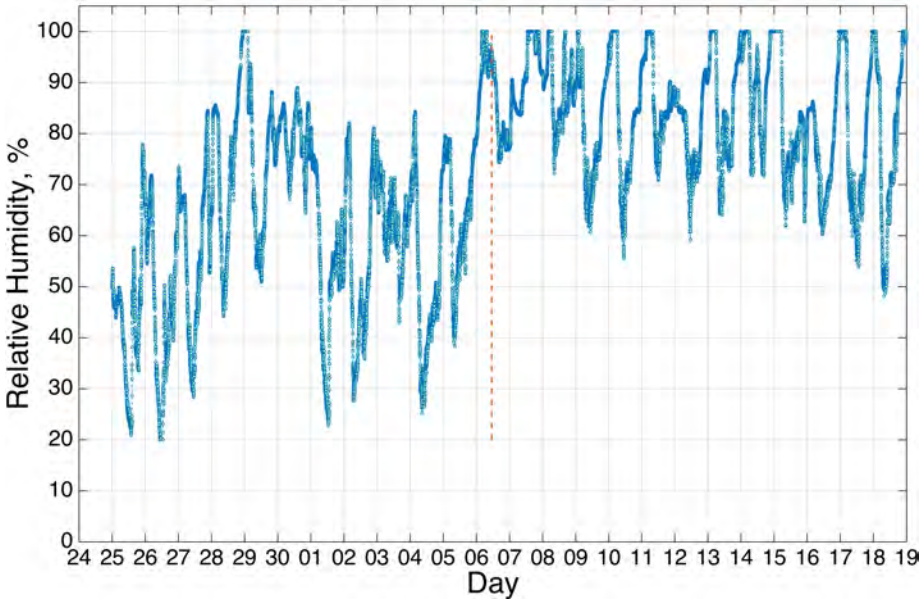

Figure 4.6: The relative humidity during the measurement.

4.1.3 Evaporation rate

The evaporation rate can be calculated with Equations (3.13) and (3.14).
A problem is that the temperature of the water was never measured during this period but later measurements in the same environment show that the water holds a temperature approximately 2 °C below the air temperature so that was used in the following calculations. Now, from Equation 3.13 the saturation vapor pressure can be calculated

$$\begin{aligned} e_s^{air} &= 0.61 \cdot \exp\left(\frac{17.3^{air}}{237.3 + T^{air}}\right) \\ e_s^{water} &= 0.61 \cdot \exp\left(\frac{17.3 \cdot (T^{air} - 2)}{237.3 + (T^{air} - 2)}\right) \end{aligned} \tag{4.1}$$

substituting this in Equation (3.14) give

$$\begin{aligned} E = 0.313 \cdot (&0.61 \exp\left(\frac{17.3 \cdot (T^{air} - 2)}{237.3 + (T^{air} - 2)}\right) - \\ &- r \cdot 0.61 \exp\left(\frac{17.3 \cdot T^{air}}{237.3 + T^{air}}\right)) \cdot (0.253 + 0.06 \cdot V) \end{aligned} \tag{4.2}$$

The wind speed $V(t)$ in the tube can be assumed to be 0 so we end up with

$$\begin{aligned} E = 0.313 \cdot (&0.61 \exp\left(\frac{17.3 \cdot (T^{air} - 2)}{237.3 + (T^{air} - 2)}\right) - \\ &- r \cdot 0.61 \exp\left(\frac{17.3 \cdot T^{air}}{237.3 + T^{air}}\right)) \cdot (0.253) \end{aligned} \tag{4.3}$$

To be able to compare the measurements with the result from equation (4.3) we need to convert the rate of change of the water surface in cm/minute to kg/m^2/hour. A portion of the water surface dh m has a volume of $V = dh\pi r^2$ m^3 and will have a weight of $1000V$ kg. During the hole period the water surface decreased 2.5 cm which mean that the total volume of evaporated water was

$$\begin{aligned} V_{tot} &= 0.025\pi \cdot 0.06^2 \\ &= 0.282 \cdot 10^{-3} \text{ m}^3. \end{aligned} \tag{4.4}$$

or in kilograms of water

$$= 0.282 \text{ kg}. \tag{4.5}$$

If we divide with the area we get

$$\begin{aligned} &= \frac{0.282}{0.06^2 \cdot \pi} \\ &= 24.93 \text{ kg/m}^2 \end{aligned} \tag{4.6}$$

This was during a period of 23 days so we finally divide by $23 \cdot 24$ to get the right unit.

$$\begin{aligned} \bar{E}_{meas} &= \frac{24.93}{23 \cdot 24} \text{kg/m}^2 \cdot \text{h} \\ &= 0.0451 \text{ kg/m}^2 \cdot \text{h} \end{aligned} \tag{4.7}$$

The resulting E in Figure 4.9 show the function surface for E as a function of the relative humidity (r) and temperature (T). The red dot represent the $\bar{E}_{meas}$ and lies just over the function surface. We now calculate the E(t) for each of the periods to see if the estimated models also coincide with this theory.

$$\begin{aligned} W_a &= -8.37 \cdot 10^{-5} x + m_1 \rightarrow 0.05022 \text{ kg/m}^2 \cdot \text{h} \\ W_b &= -6.12 \cdot 10^{-5} x + m_2 \rightarrow 0.03672 \text{ kg/m}^2 \cdot \text{h} \end{aligned} \tag{4.8}$$

These are represented in Figure 4.9 as the blue and green dot respectively. Figure 4.10 show a slice of the function surface at $T = 22.1$ °C together with W_a and W_b. They both fit well to the theoretical data and we can conclude that the change in the rate of the water surface surely depend on the change in the mean relative humidity during the latter period.

4.1.4 Repeatability

The two models can now be used to detrend the data set and calculate the statistics. Thus, using Equation (3.1) the repeatability of the bubbler unit is found to be $\sigma = 0.010$ cm. In the data set plotted in Figure 4.11 the two trends are subtracted from the original data. The dotted lines represent σ.

4.1.5 Linearity

A test of the linearity was performed by measure at a specific water level then manually adding water in the tube and once again sample about 20 samples from the bubbler. The result can be seen in Figure 4.7. The horizontal lines represent the manually read values for each measurement, using a tape measure. If the manually read values are subtracted from each measurement we get the result shown in Figure 4.8. It clearly show that something happened during the measurement when the bubbler unit suddenly started to scatter the samples. The problem persist despite several attempts to sort it out by changing the air tube and all of the surrounding electronics. Leading to the conclusion that the unit failed. It was later returned to the manufacturer. However if the linearity is calculated using the measurements before the failure (measurement 1– 5) and the theory in Section 3.2 is used we get

$$lin_{\%} = 0.022 \ \% \tag{4.9}$$

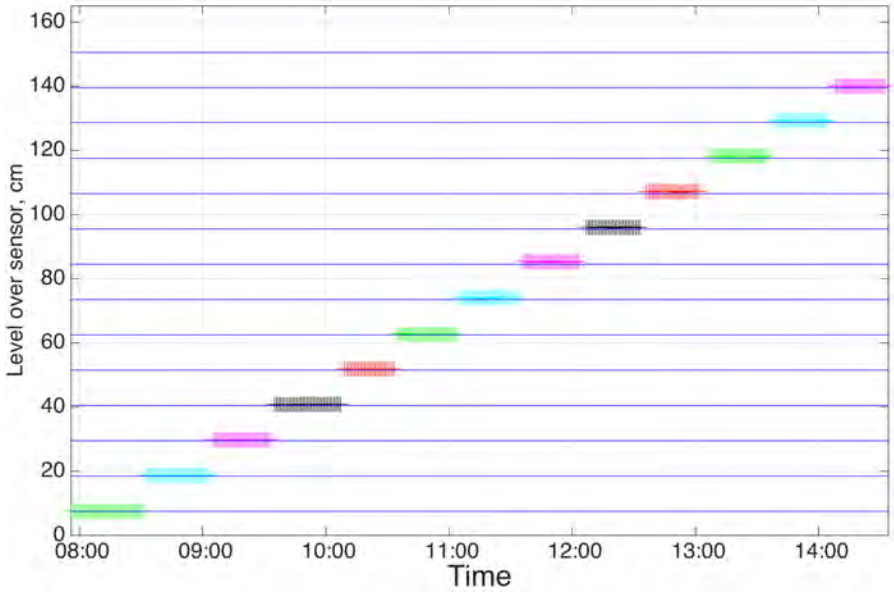

Figure 4.7: The raw data from the linearity measurement. The horizontal lines represent the manually read value.

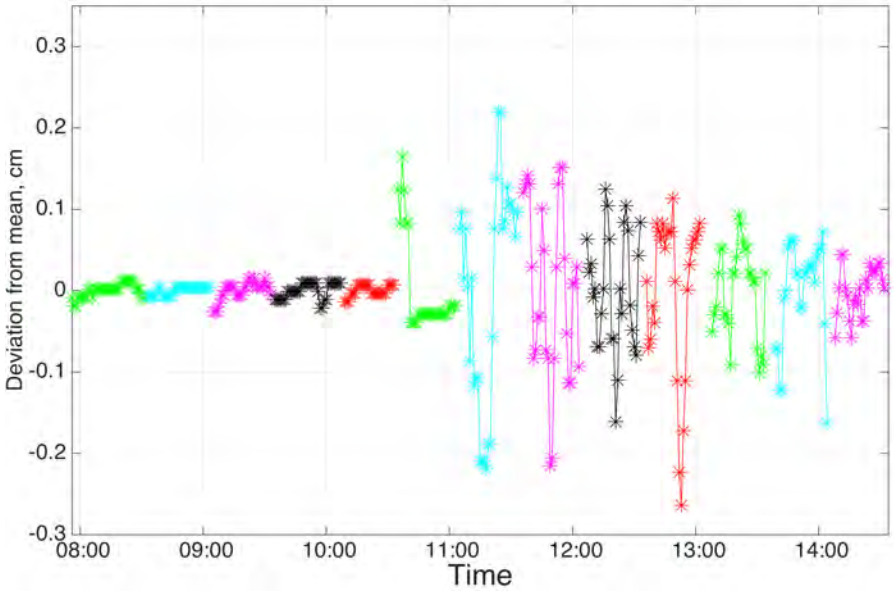

Figure 4.8: Each level with the manually read value subtracted.

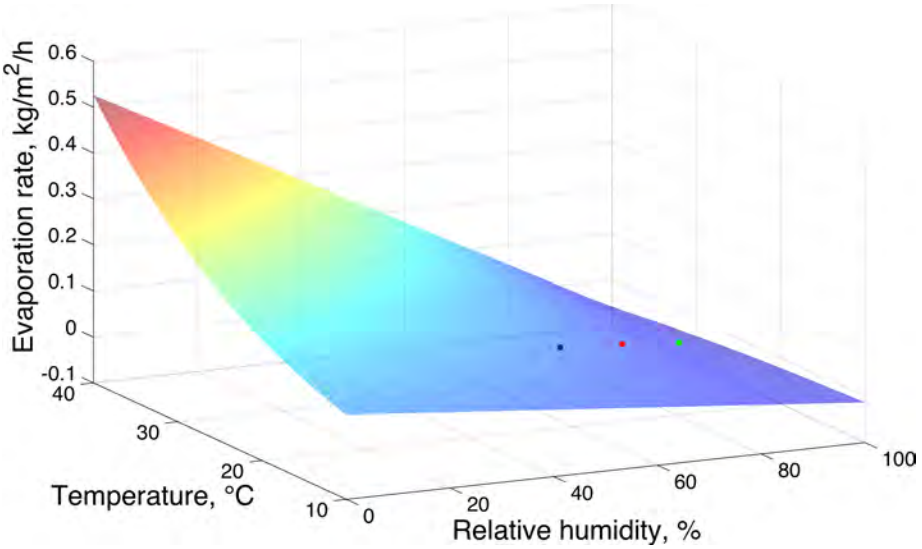

Figure 4.9: The function surface $E(t)$ with the mean evaporation rate for the whole measurement period marked with the red dot, W_a is marked with the green dot and W_b with the black dot.

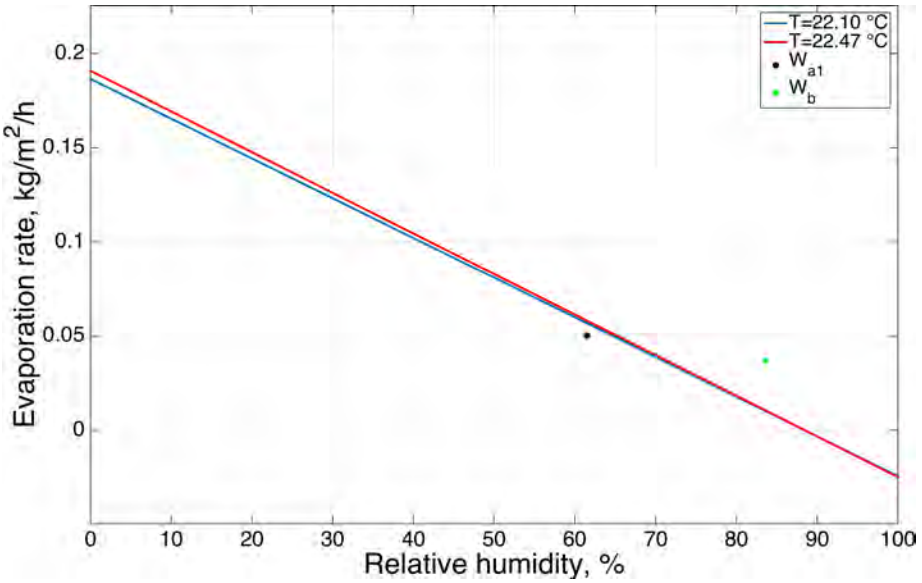

Figure 4.10: A slice of the evaporation rate E(t) at the two mean temperatures of the periods. The green and black dot represent W_a and W_b, respectively.

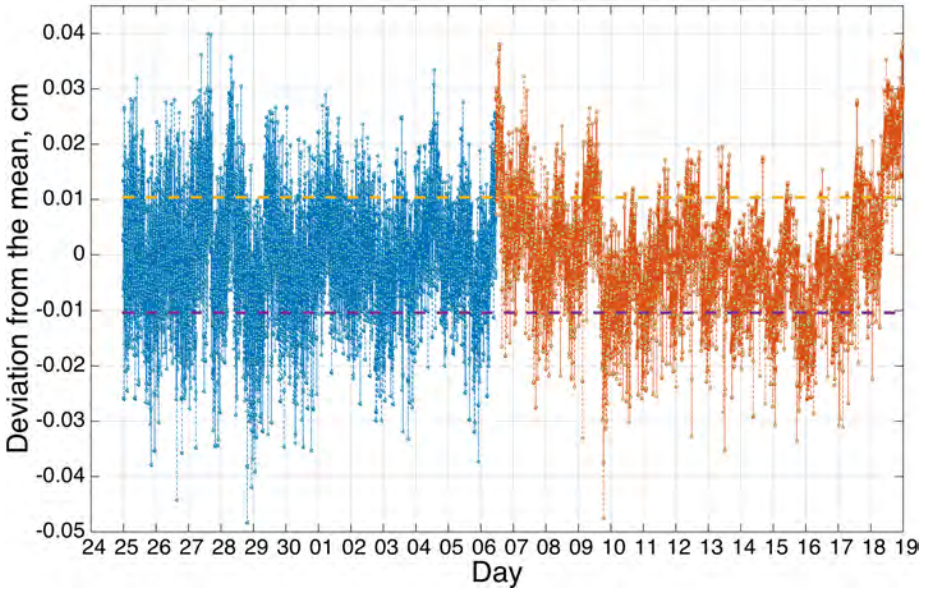

Figure 4.11: The data from Figure 4.4 with the trend subtracted. Period 1 represented in blue and period 2 in brown. Plus/minus one standard deviation (0.010 cm) is marked with the two dashed lines.

4.2 Radar sensor

4.2.1 Experiment setup

Four different setups were used during the measurements with the radar unit.

- Setup 1, The radar unit placed in a tube. This setup was used to measure how the radar perform in an environment with a lot of reflections.
- Setup 2, The radar unit placed over a wheelbarrow. Used for close range measurements.
- Setup 3, The radar unit placed on a table over a plastic pool. Used to measure on a more realistic range.
- Setup 4, The radar unit placed over a plastic pool. Used to measure with an angular offset.

4.2.2 Long term measurement

The next experiment was performed in an 18 day period between the 30th of April to the 17th of May. The result can be seen in Figure 4.12. With the trend due to evaporation subtracted from the data we end up with Figure 4.13. A clear sine formed signal is present in the data. Further investigation revealed that the signal was dependent on the position of the water surface and is probably due to reflections in the side walls of the plastic tube used in the experiment and therefore dependent of the position of the water surface. When the water evaporate the surface slowly descend and change the reflection conditions in the tube. The change in rate of evaporation found in the experiments with the bubble unit, caused by the change of relative humidity, is reflected in the change of period time in the sine formed signal. The period become longer, indicating a slower descend of the water surface, as the relative humidity increase. The variation has a period of about 6 days. The theory of evaporation discussed in Section 3.4 can be used to find the relationship between the descending water surface and period time. Using the result from Equation (4.3), repeated below, the evaporation during the two periods can be estimated by using the mean temperature and relative humidity during the measurement.

$$\begin{aligned} E = 0.313 \cdot (0.61 \exp\left(\frac{17.3 \cdot (T^{air} - 2)}{237.3 + (T^{air} - 2)}\right) - \\ - r \cdot 0.61 \exp\left(\frac{17.3 \cdot T^{air}}{237.3 + T^{air}}\right)) \cdot (0.253) \end{aligned} \tag{4.10}$$

substituting the temperature of the air, T^{air}, with 22 °C and the relative humidity, r, with 60 % for the first period. And with 22 °C and 80 % for the latter one and assuming that the water temperature is 2 °C lower than the air we get

$$\begin{aligned} E_{period1} &= 0.0596 \text{ kg/m}^2 \cdot \text{h} \\ E_{period2} &= 0.0177 \text{ kg/m}^2 \cdot \text{h} \end{aligned} \tag{4.11}$$

Since we know the tube radius recalculating the value to difference in the position of the water surface can now be done. The area of a slice of water in the tube is $A_{tube} = 0.2^2 \cdot \pi$ which multiplied with the result from Equation (4.12) the give the rate in kg per hour for our tube. From the fact that $V = A \cdot h$ and that $V = weight/\rho$ the height of the evaporated water can be calculated as $h = weight/\rho \cdot A$

$$\begin{aligned} E_{period1} &= 0.0075 \text{ kg/h} \\ E_{period2} &= 0.0022 \text{ kg/h} \end{aligned} \tag{4.12}$$

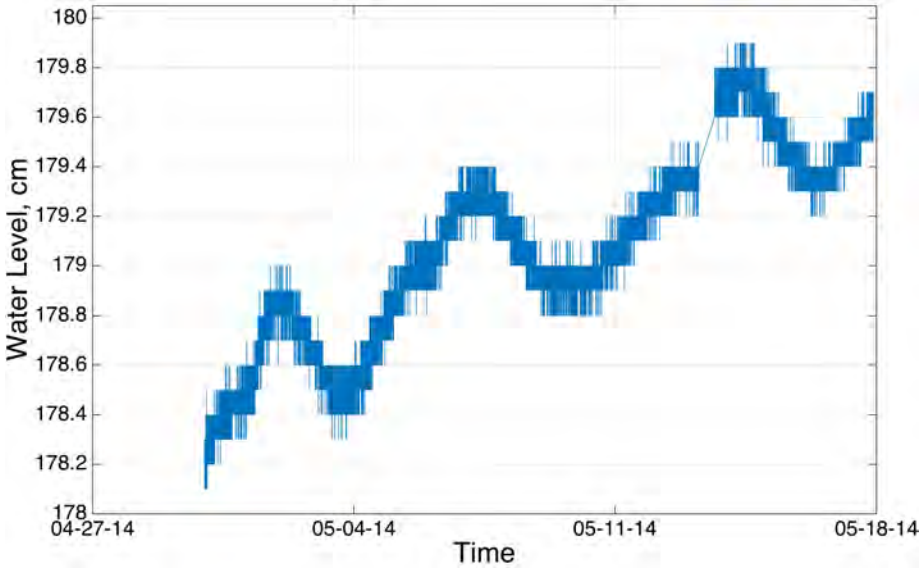

Figure 4.12: The sine formed signal due to movement of the water surface induced by evaporation.

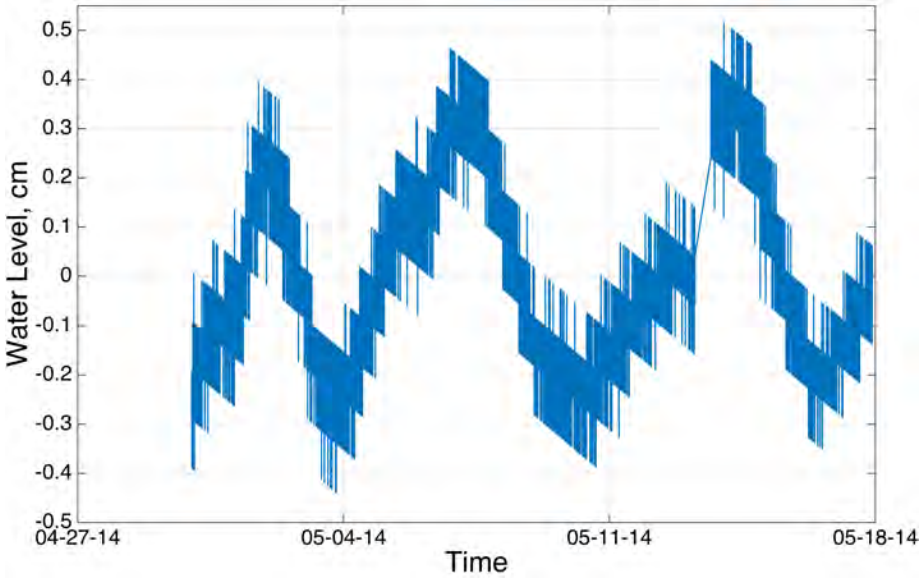

Figure 4.13: The sine formed signal from Figure 4.12 with the trend subtracted.

4.2.3 Close range measurement

The radar has a nominal range from 50 mm to 20 m. It is unclear if the 50 mm are calculated from the the end of the horn or from the reference plane at the beginning of the horn. Figure 4.14 show the radar horn placed just over the water surface. The result from several measurements with the radar horn placed at 5 mm to 200 mm from the water surface can be seen in Figure 4.16 and without the trend in Figure 4.17 were it is clear that measurements as close as 0.5 mm from the end of the radar horn are possible. During the measurements the radar was manually moved between the consecutive measurement points and the height was monitored by means of a tape measure glued to the side of the construction (Figure 4.15). A linearity of $Lin_{\%} = 0.015$ % was found.

Figure 4.14: The radar horn placed just over the water surface ($d = 5$ mm).

Figure 4.15: The measurement aid; a glued tape measure.

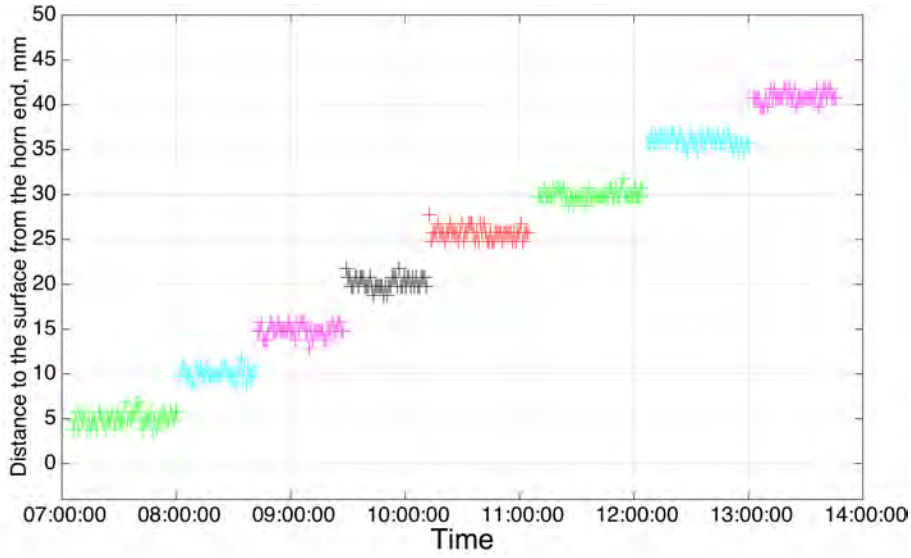

Figure 4.16: The result from measurements between 5 – 40 mm. Each of the levels contain about 20 samples and the mean of the standard deviation for each level is 0.65 mm.

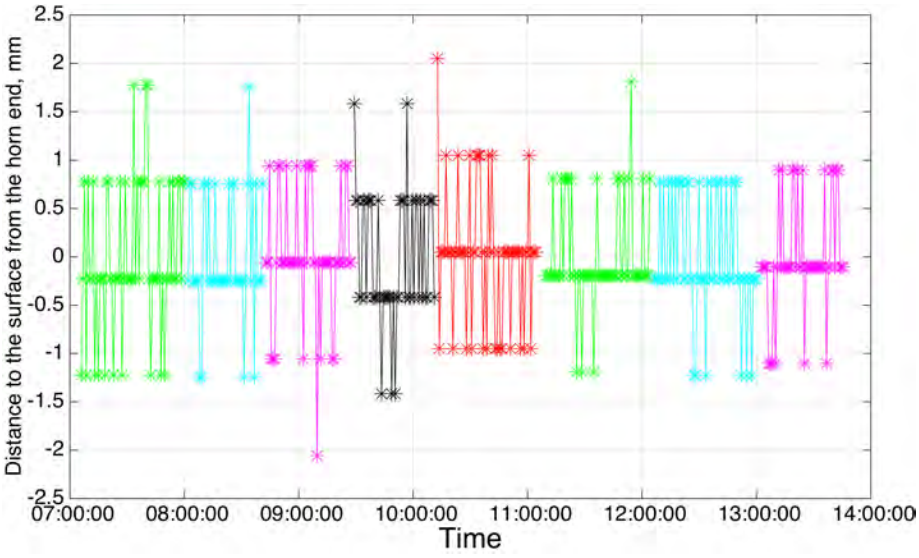

Figure 4.17: The data in Figure 4.16 without the trend.

4.2.4 Sensitivity to angular offset

An angular offset should decrease the received reflected energy of the transmitted radar pulse, possibly introducing an error in the distance to surface measurement. The following section describe an experiment with the radar mounted on a pedestal over a plastic pool (Figure 4.19). The angle was measured with an inclinometer, Clinotronic PLUS from Wyler AG, Switzerland (Figure 4.20). With a nominal error limit of 1 arcmin + 1 digit (Appendix F). The radar has a beam angle of 8 deg which at 0.8 m height give a footprint of 0.2 m. Two experiments were performed. Each of them started at the reference angle with the radar pointing in nadir. Then was shifted with 2° each measurement until, in the first experiment, 12° and in the second 8°. As a reference a tape measure was used. Figure 4.18 show the mean deviation from the reference as a function of the angle from nadir. The systematic error in the first experiment could be due to the way the reference measure were performed. Notable is the approximately 5 mm underestimation of the distance at 6° since we expect the distance to increase with angle which is the case for the rest of the angles. But since the side lobes of the antenna are unknown we do not know if they could explain the behavior.

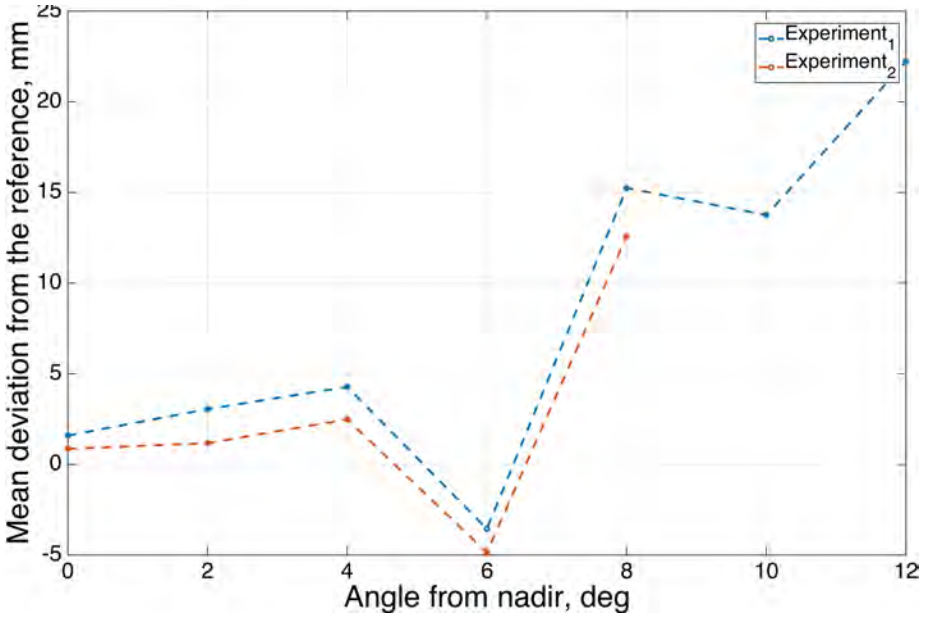

Figure 4.18: The mean deviation from the reference as a function of angle from nadir for the two measurements.

Figure 4.19: The radar placed above the pool with the inclinometer placed on top. The unit is mounted on a plate which is moveable in all directions.

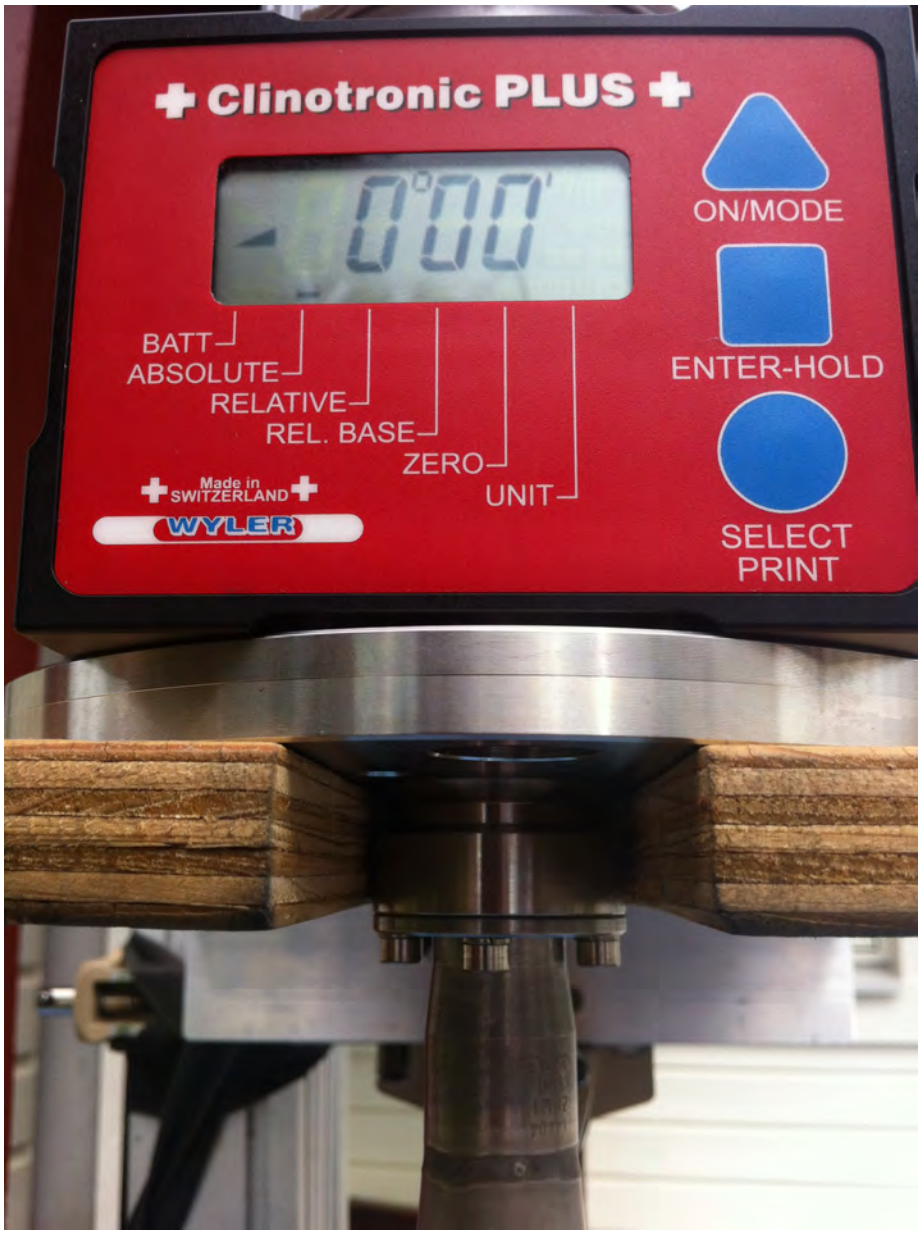

Figure 4.20: The inclinometer.

Chapter 5

Field experiments

5.1 Introduction

In this Chapter we investigate the performance of the sensors in a more realistic environment. The equipment was moved to the newly constructed measurement well at the shoreline not far from the 25 metre telescope(see Figure 5.1 to Figure 5.4). Nearby is an old hut which is used to house the bubble units, backup batteries and data acquisition units. The data acquisition units deliver their data to the main server at the observatory through a fiber optical communication line. Each unit has its own backup battery to ensure a continues operation.

5.1.1 The site

The final site of the installation, the measurement well, can be seen in Figure 5.2. The well is constructed by a concrete tube with a inner insulated plastic tube. Three pipes in the bottom of the well let the sea water flow freely in and out of the well. The radar unit is placed on a steel tripod, see Figure 5.5, centered in the well. The bubbler nozzle is fastened in the tube wall near the bottom. A heater to keep the air temperature above zero degrees is attached on the inner plastic tube wall. The electronics and data gathering equipment are placed in the measurement hut and a plastic pipe run, with all the cables and the air tubes to the bubble units, from the measurement hut into the well.

Figure 5.1: The new measurement well and the measurement hut before the installation of the sensors.

Figure 5.2: The new measurement site.

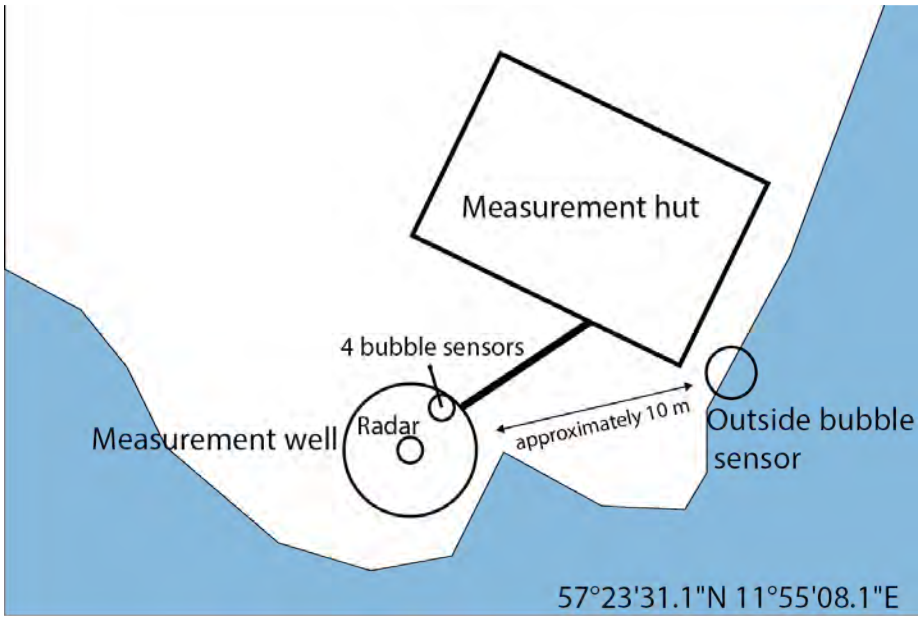

Figure 5.3: An overview of the measurement site.

Figure 5.4: An overview of the measurement site.

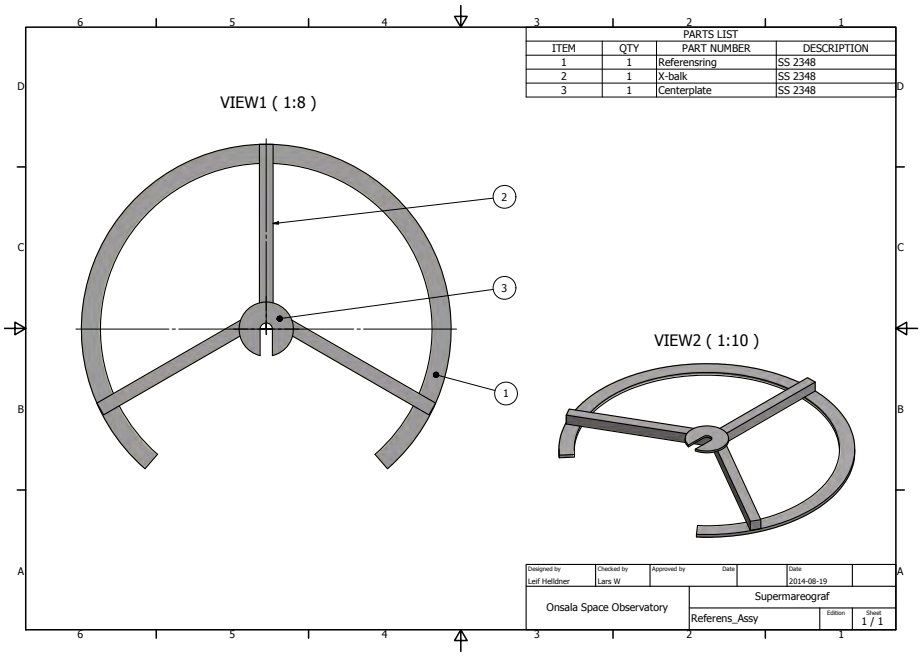

Figure 5.5: The radar tripod.

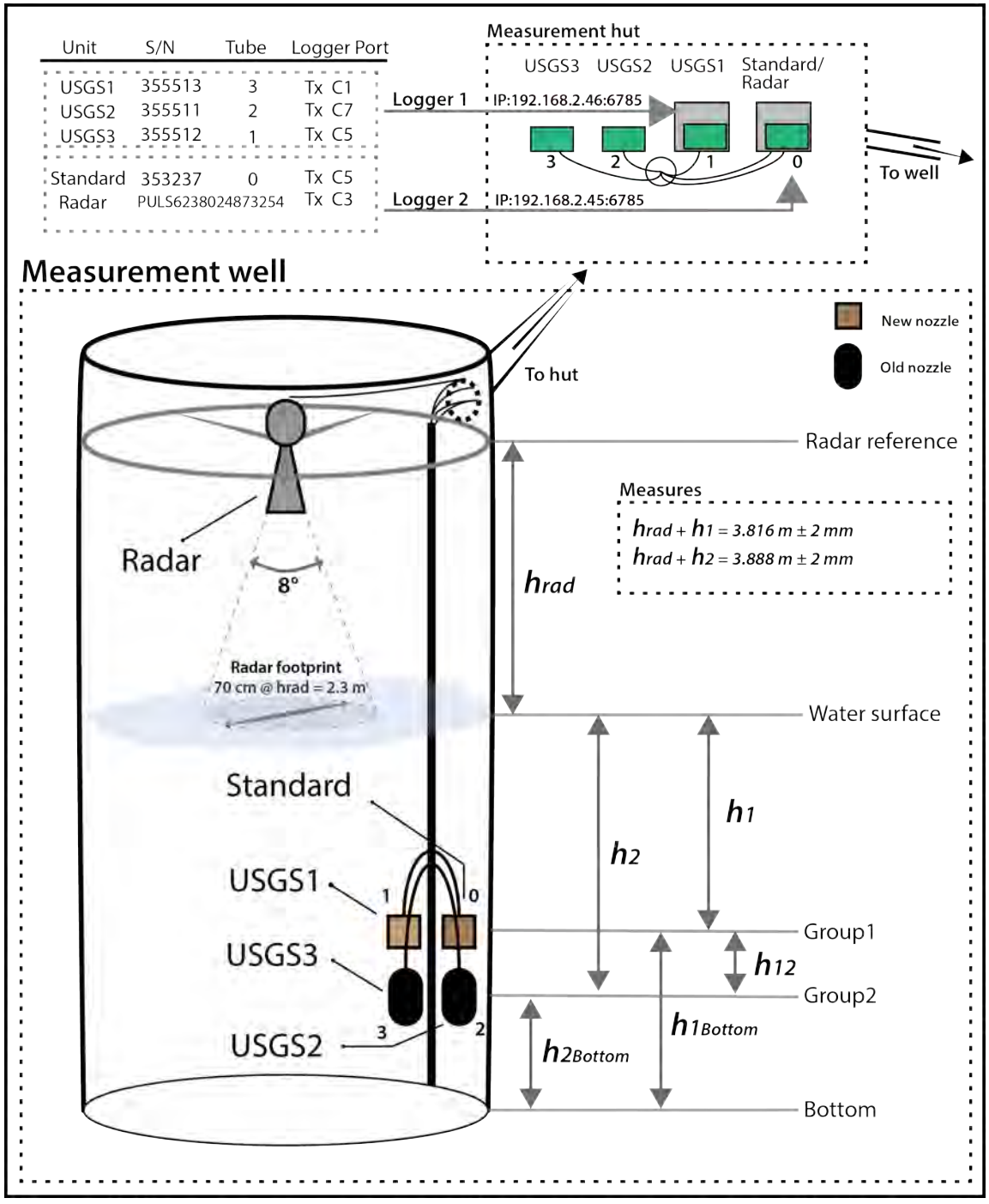

Figure 5.6: A schematic view of the measurement well and the placement of the data acquisition units for each sensor in the measurement hut.

5.1.2 Sensor location

Figure 5.6 show a schematic view of the measurement well, the measurement hut, the plastic tube connection them and the current location of the outside sensor.

5.1.3 A new type of bubbler unit

In the field experiments three of the four bubbler units in the well were of a new, more accurate type. The new bubbler units will be referred to as USGS (U.S Geological Survey). The nominal accuracy of the new type is 1 mm in the interval $0.5 - 3$ m compared to 3 mm in the same interval for the standard units used in the indoor experiments. The differences between the new and old units are investigated in the field experiments.

5.1.4 Two types of nozzles

The bubbler units are delivered with a streamlined plastic nozzle fitted with a ball joint. The ball joint make it possible to move the nozzle about 15° in each direction. This is a desired feature if the installation requires an adjustment of the nozzle to be horizontal. But there is also a drawback, there is a risk of accidentally moving the joint, e.g during maintenance work, and thereby change the reference height. Therefore a new type of nozzle was constructed and fitted to two of the four units. The new nozzles are made of a block of copper with drilled holes working as a bubble chamber. All four nozzles can be seen in Figure 5.7 placed on a steel rod which then is submerged in the well and fastened to the side wall. The numbering on the nozzles can be matched to the bubbler units in the measurement hut according to Figure 5.6.

Figure 5.7: The two types of nozzles fastened to a steel rod just before they were installed in the well.

5.2 Raw data

5.2.1 Linearity experiment

Two experiments of the linearity were performed. The first on October 11 and the second on December 2. The well was filled with water and then drained at intervals of $20 - 30$ cm. About 20 samples per level were collected.

5.2.2 Long term experiment

In the long the experiment the raw data from the radar and the bubble sensors consist of two periods; the first from December 4 to December 31st 2014 and the second the entire month of Januari 2015. They are shown in Figure 5.8 and Figure 5.9 respectively. A storm hit the coast of Sweden on the afternoon of January 10th with water levels up to one metre from the radar reference therefore the data set contains a large dynamic range with both calm periods as around the 21st and stormy periods as around the 10th.

Figure 5.8: The raw data from the 4 bubble sensors in the well, which in this plot fall on top of each other, and the bubble sensor outside the well together with the radar. Since the radar measure the distance from above down to the water surface the data is inverted in respect to the bubble sensor data. The bubble sensors in the well are paired into two groups were one group is fitted with the new nozzle and placed at height $hrad + h_1$ and the other with the original nozzle and placed at height $hrad + h_2$.

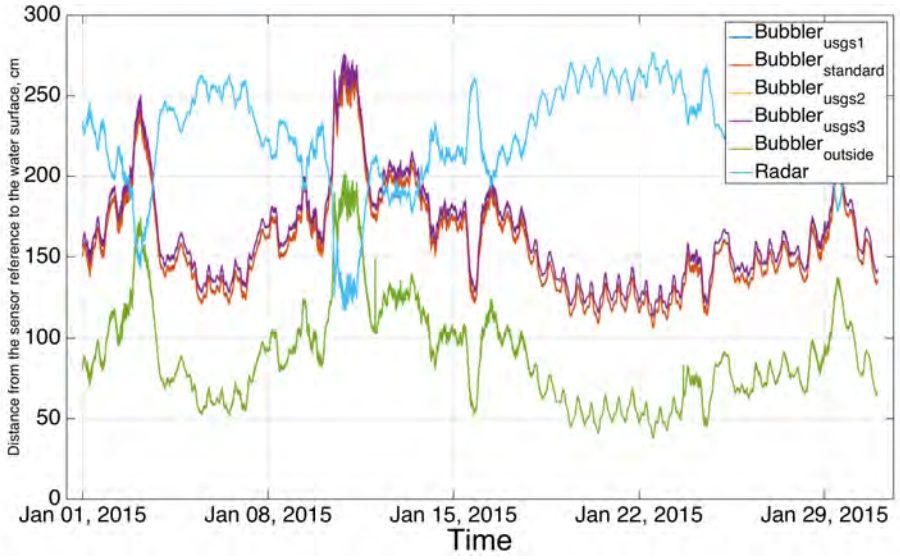

Figure 5.9: The raw data from the 4 bubble sensors in the well and the bubble sensor outside the well together with the radar. Since the radar measure the distance from above down to the water surface the data is inverted in respect to the bubbles sensor data. The bubble sensors in the well are paired into two groups were one group is fitted with the new nozzle and placed at height $hrad + h_1$ and the other with the original nozzle and placed at height $hrad + h_2$.
.

5.3 Bubble sensors performance

Figure 5.10 is a zoomed version of the raw data and show the four bubble sensors, paired into two groups at two different heights. Since we are interested in the performance of each sensor Figure 5.11 shows the difference between the sensors internally in the groups. They are obviously less correlated during the storm and the difference between bubble sensor 1 and the non USGS sensor are much larger than the difference between the USGS sensors 1 and 2. Figure 5.12 show the difference between the USGS sensors regardless of the groups and even if the differences are smaller than between the non-USGS and bubble sensor 1 they are still striking. As a reference we can compare with the sensor outside the well. Figure 5.13 show that during a period with more water movement the correlation between two bubbler units placed in the well, separated just by a couple of centimetres are almost the same as the correlation between the same bubbler unit and the one outside the well. If the radar is used as the true reference we get the plot in Figure 5.14 which show the difference between each sensor and the radar. To put numbers on this difference the standard deviation is calculated below. Surprisingly the smallest deviation is the one between the radar and the normal Bubble unit. However, this strengthens the suspicion that the sample time of the bubble units are not perfectly matched. The only thing that can make the normal unit better correlated with the radar would be better timing and since the standard bubble sensor unit and the radar are the only ones that share data acqusition unit. The conclusion is that the timing differs between the other units and the radar.

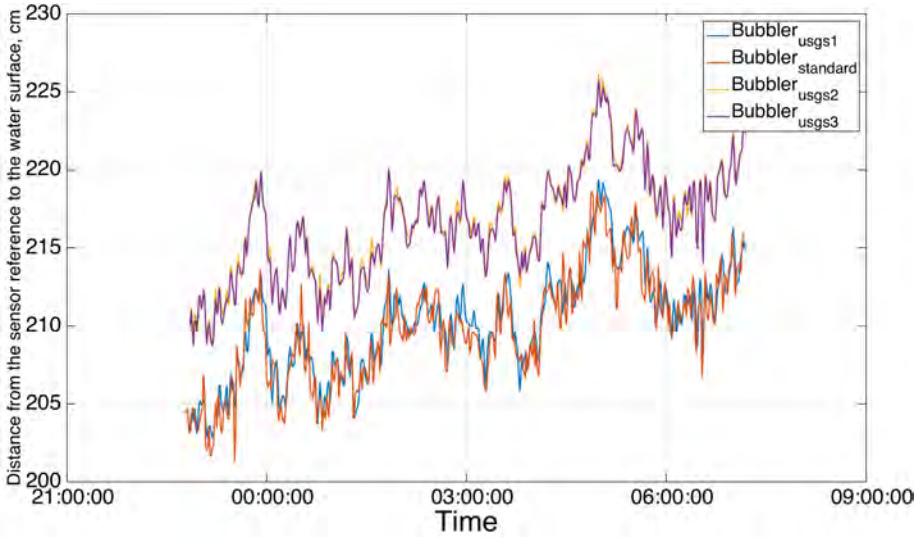

Figure 5.10: A zoom of Figure 5.9. The two groups of bubble sensors with $Bubbler_{usgs1}$ and $Bubbler_{Standard}$ at height $hrad + h_1$and $Bubbler_{usgs2}$ and $Bubbler_{usgs3}$ at height $hrad + h_2$.

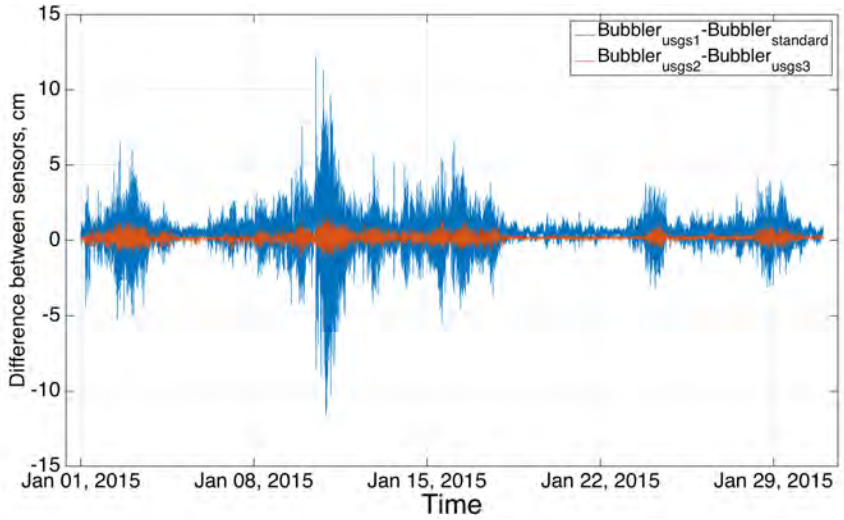

Figure 5.11: The internal difference in each group.

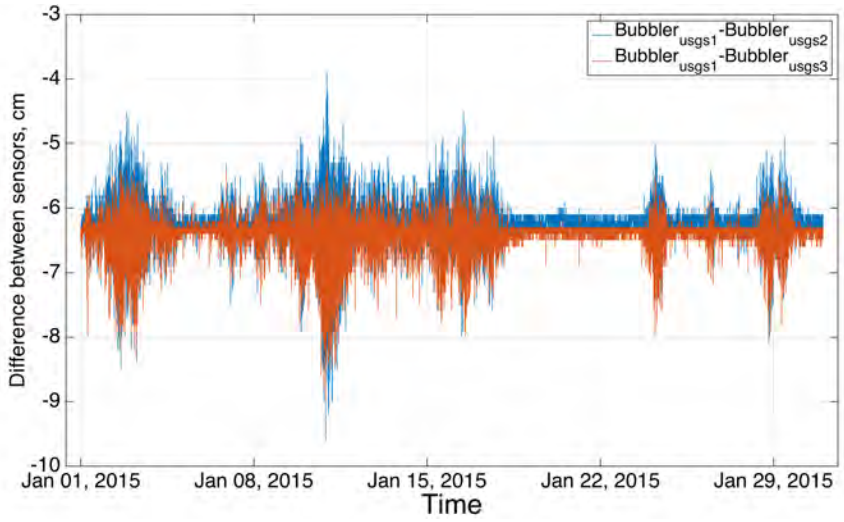

Figure 5.12: The difference between the USGS bubblers.

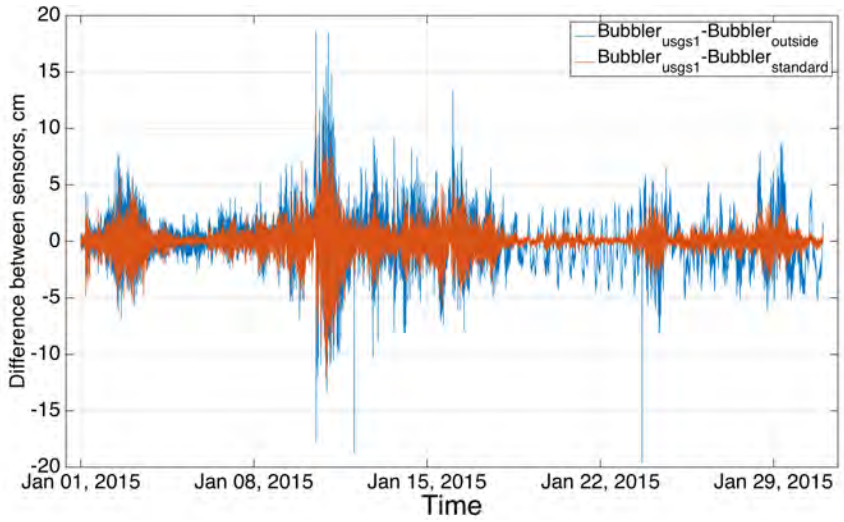

Figure 5.13: The difference between one of the USGS bubblers and the normal bubbler in the well compared to the difference between the same USGS bubbler and the bubbler outside the well.

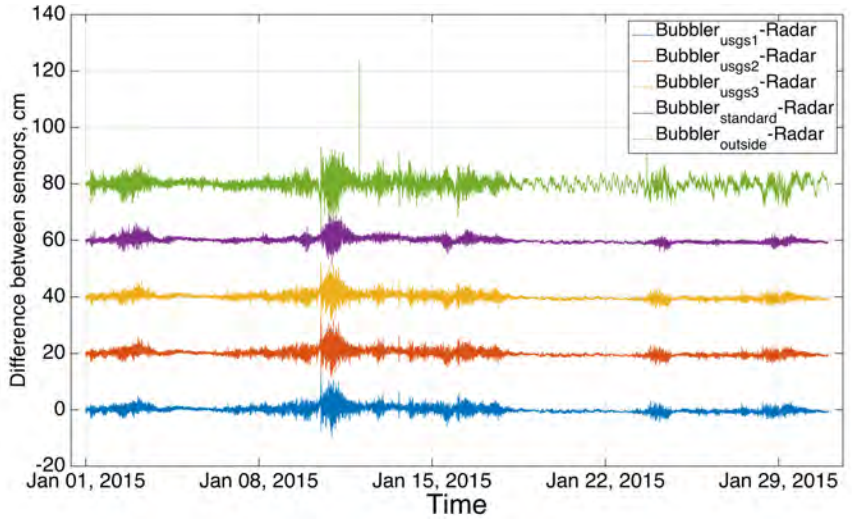

Figure 5.14: The difference between all bubble sensors and the radar. An offset of 20 cm is applied to distinguish the sensors.

Table 5.1: The December statistics of the differences between the bubble units and the radar.

Sensors	Mean (cm)	SD (cm)
$\text{Bubbler}_{usgs1} - Radar$	383.86	1.07
$\text{Bubbler}_{usgs2} - Radar$	390.29	1.08
$\text{Bubbler}_{usgs3} - Radar$	390.09	1.08
$\text{Bubbler}_{standard} - Radar$	383.46	0.64
$\text{Bubbler}_{outside} - Radar$	314.38	1.45

Table 5.2: The December statistics of the differences between the bubble units.

Sensors	Mean (cm)	SD (cm)
$\text{Bubbler}_{usgs1} - Bubbler_{standard}$	0.4	1.05
$\text{Bubbler}_{usgs2} - Bubbler_{usgs3}$	0.19	0.15
$\text{Bubbler}_{usgs1} - Bubbler_{usgs2}$	−6.43	0.18
$\text{Bubbler}_{usgs1} - Bubbler_{usgs3}$	−6.24	0.21
$\text{Bubbler}_{usgs1} - Bubbler_{outside}$	69.48	1.81

Table 5.3: The December statistics of the differences between the sensors in the well and the sensor outside the well.

Sensors	Mean (cm)	SD (cm)
$\text{Bubbler}_{usgs1} - Bubbler_{outside}$	69.48	1.81
$\text{Bubbler}_{usgs2} - Bubbler_{outside}$	75.91	1.81
$\text{Bubbler}_{usgs3} - Bubbler_{outside}$	75.72	1.82
$\text{Bubbler}_{standard} - Bubbler_{outside}$	69.08	1.46
Radar- $\text{Bubbler}_{outside}$	−314.38	1.45

Table 5.4: The January statistics of the differences between the bubble units and the radar.

Sensors	Mean (cm)	SD (cm)
$\text{Bubbler}_{usgs1} - Radar$	383.71	1.07
$\text{Bubbler}_{usgs2} - Radar$	390.13	1.09
$\text{Bubbler}_{usgs3} - Radar$	389.97	1.09
$\text{Bubbler}_{standard} - Radar$	383.27	0.93
$\text{Bubbler}_{outside} - Radar$	314.18	1.99

Table 5.5: The January statistics of the differences between the bubble units.

Sensors	Mean (cm)	SD (cm)
$\text{Bubbler}_{usgs1} - Bubbler_{standard}$	0.44	0.99
$\text{Bubbler}_{usgs2} - Bubbler_{usgs3}$	0.16	0.18
$\text{Bubbler}_{usgs1} - Bubbler_{usgs2}$	−6.42	0.23
$\text{Bubbler}_{usgs1} - Bubbler_{usgs3}$	−6.26	0.29
$\text{Bubbler}_{usgs1} - Bubbler_{outside}$	69.53	2.12

Table 5.6: The January statistics of the differences between the sensors in the well and the sensor outside the well.

Sensors	Mean (cm)	SD (cm)
$\text{Bubbler}_{usgs1} - Bubbler_{outside}$	69.53	2.12
$\text{Bubbler}_{usgs2} - Bubbler_{outside}$	75.95	2.13
$\text{Bubbler}_{usgs3} - Bubbler_{outside}$	75.79	2.13
$\text{Bubbler}_{standard} - Bubbler_{outside}$	69.09	2.02
Radar- $\text{Bubbler}_{outside}$	−314.18	1.99

5.4 Van de Casteele diagrams

One way to compare the sensors is to plot the difference between a reference and a sensor against the reference value. We expect the difference between the reference and the sensor to be constant regardless of in which interval we measure. The bubbler units are dependent on the correct water density to be able to make a correct measurement of the depth in contrast to the radar unit which just measure the reflected energy from the water surface. Figure 5.15 to 5.19 show the Van de Casteele diagrams of the bubble sensors and the radar. If we look at the data from December, Figure 5.15 and 5.17, and especially take a closer look at the data from the standard bubble sensor compared with the radar shown in Figure 5.16. There is a wave like shape at around -280 to -260 cm, and we recognise the behaviour from the indoor experiments. The effect is observed at a low water level which was the case in the indoor experiments as well and a theory is that this is due to reflections in the walls of the well. So if it is due to radar reflections why is it only the standard bubbler, radar, difference that show this effect? Earlier it was established that this unit was the only one that was perfectly matched in time to the radar unit and therefore show the best fit to the radar data.

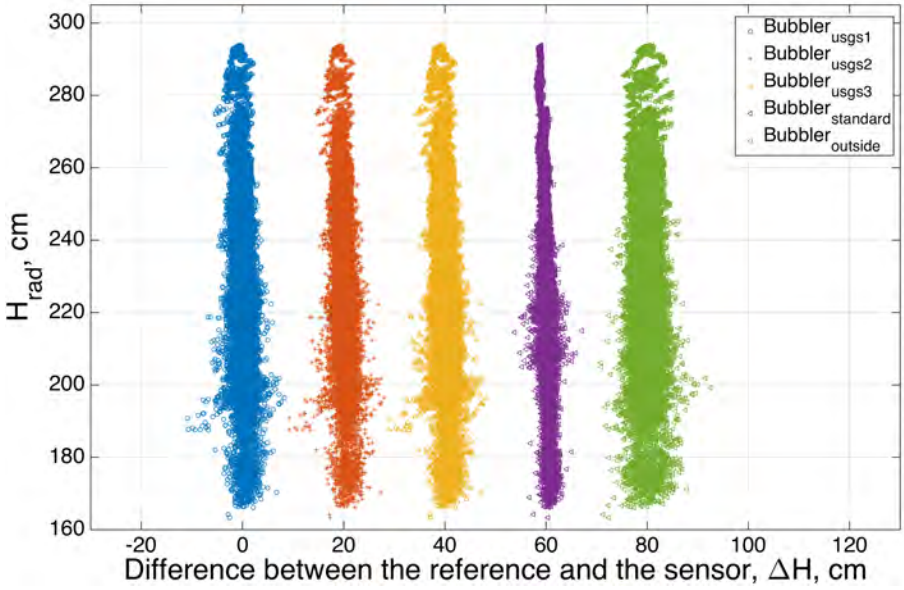

Figure 5.15: The difference between the radar and all bubble sensors as a function of the radar. Data from December 2014. The legend read top-down corresponds to the time series from left to right. A 20 cm offset has been added to the x values on each time series.

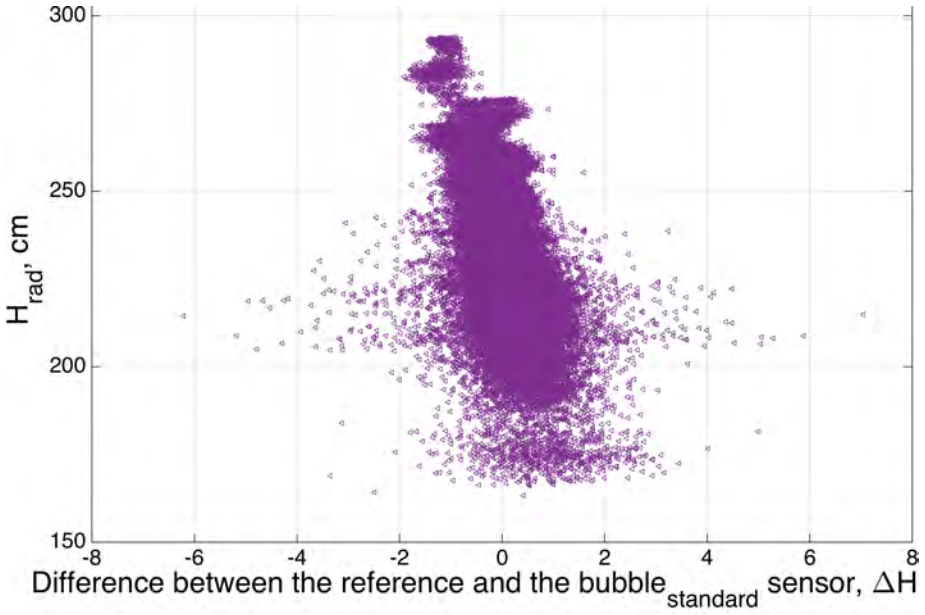

Figure 5.16: A closer look at the standard Bubble sensor from the previous figure.

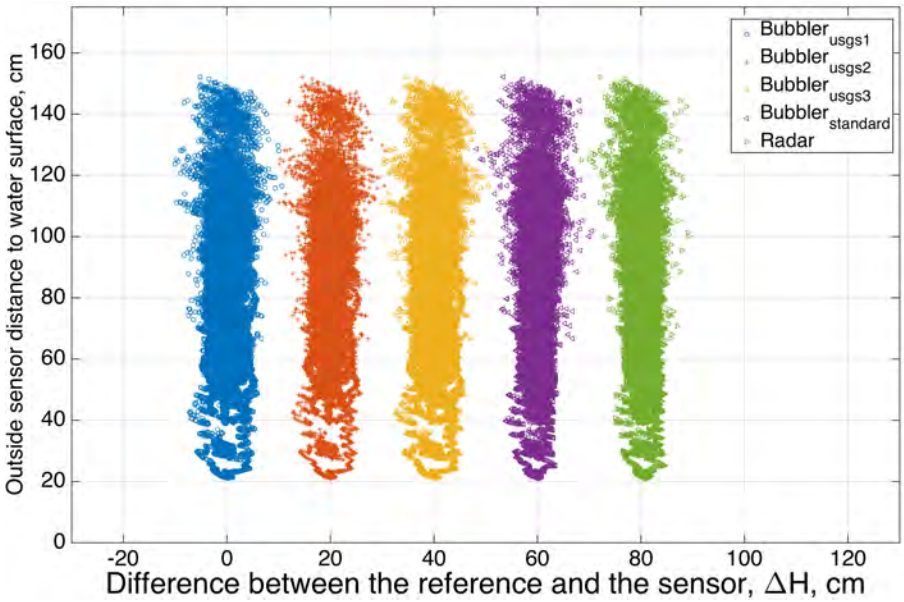

Figure 5.17: The bubble sensors as a function of the difference between the sensor outside the well and the bubble sensors. Data from December 2014. The legend read top-down corresponds to the time series from left to right. A 20 cm offset has been added to the x values on each time series.

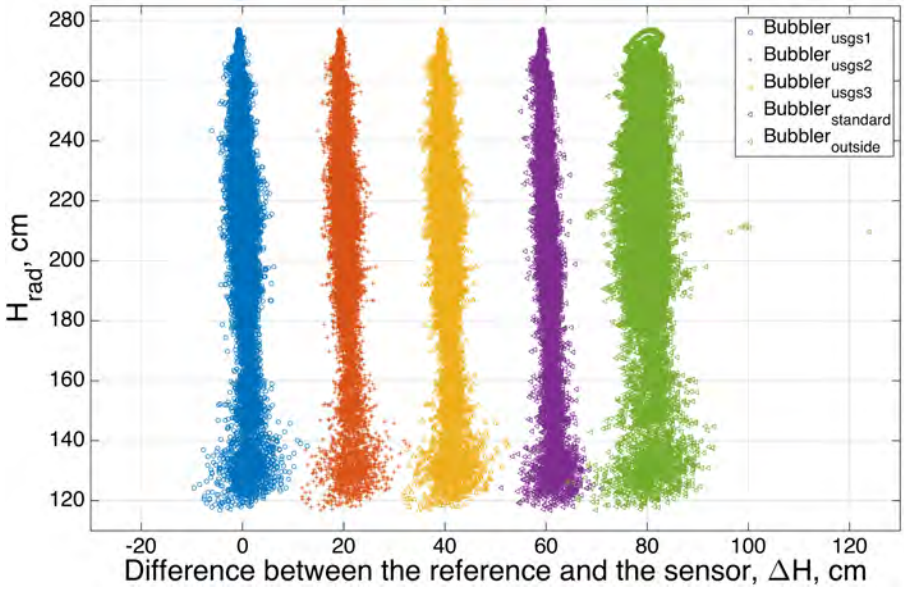

Figure 5.18: The difference between the radar and all bubble sensors as a function on the radar. Data from January 2015. The legend read top-down corresponds to the time series from left to right. A 20 cm offset has been added to the x values on each time series.

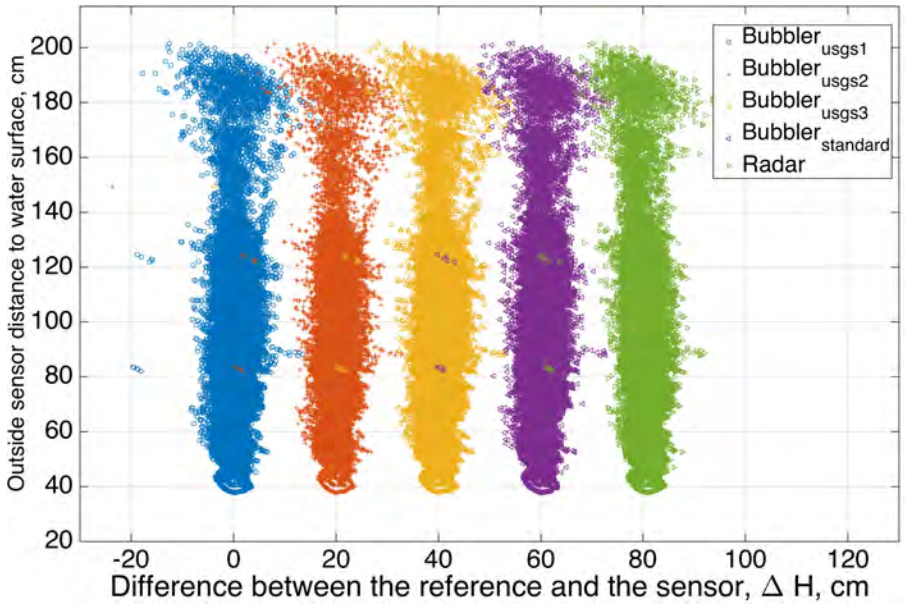

Figure 5.19: The bubble sensors as a function of the difference between the sensor outside the well and the bubble sensors. Data from January 2015. The legend read top-down corresponds to the time series from left to right. A 20 cm offset has been added to the x values on each time series.

5.5 Nozzle comparison

Figure 5.20: The new and standard nozzles.

To find out if there is a difference between the new, in-house designed nozzle (Nozzle 0 and 1 in Figure 5.20) and the standard nozzle (Nozzle 2 and 3) the residuals between the the nozzle pairs were compared. Nozzle 0 is left out in the comparisons since it is fitted with the less accurate standard bubble unit. It is hard to determine if the horizontal distance between the location of the units has a part in any measurements differences. One could suspect that since the bubbler units fires a measurement at the same time, bubbles from the lower placed units disturb the upper ones. We would like to compare the two new nozzles with each other but since one of the new nozzles is placed on the standard bubble unit that is not possible with the current setup. In future measurements it would be possible to change the units so that a comparison is possible. Tables 5.7 and 5.8 show the standard deviation of the differences. About 95 % of the data lie in the $0.4 - 0.6$ cm interval for the difference between the new and old and about 0.3 cm in the case with the difference between the old nozzles. This is no significant difference. In order to really figure out if there is a difference between the nozzles further investigation is required.

Table 5.7: The statistics of the differences between nozzles from the December data.

Nozzle pair	SD (cm)
$Nozzle_1 - Nozzle_2$	0.18
$Nozzle_1 - Nozzle_3$	0.21
$Nozzle_2 - Nozzle_3$	0.15

Table 5.8: The statistics of the differences between nozzles from the January data.

Nozzle pair	SD (cm)
$Nozzle_1 - Nozzle_2$	0.23
$Nozzle_1 - Nozzle_3$	0.29
$Nozzle_2 - Nozzle_3$	0.18

5.6 Linearity

Two measurements were made to test the linearity of the units. One on October 11 referred to as the first experiment and the other December 2 referred to as the second experiment. Both of them were made by filling the well with water and then drain 20 cm in the first experiment and 30 cm in the second for each measurement. About 20 samples at each level were gathered. A tape measure was used as a reference on both occasions with the difference that the tape measure was fastened in a carrier (see Figure 5.23) in the second experiment which made the readings easier. The accuracy of a reading from the tape measure is estimated to ± 1 mm.

5.6.1 The first experiment, October 11 2014

Figure 5.21 show the mean distance to the water surface at each measurement level. The radar and the standard bubble sensor which were the only ones installed in the well at this point both deviate from the reference which is more clear in Figure 5.22 which show the difference between the reference and the mean of the sensor level for each interval.

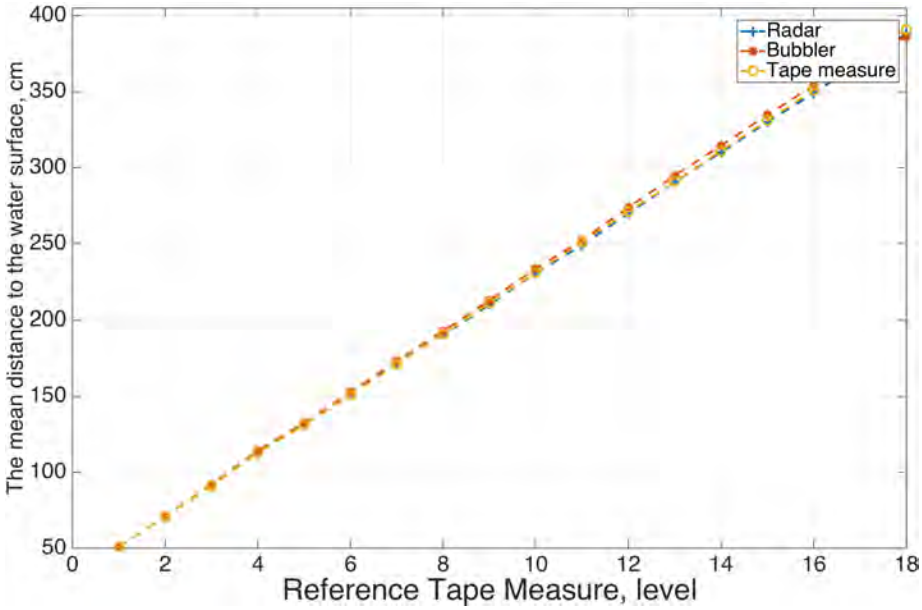

Figure 5.21: The mean for each level together with the reference tape measure.

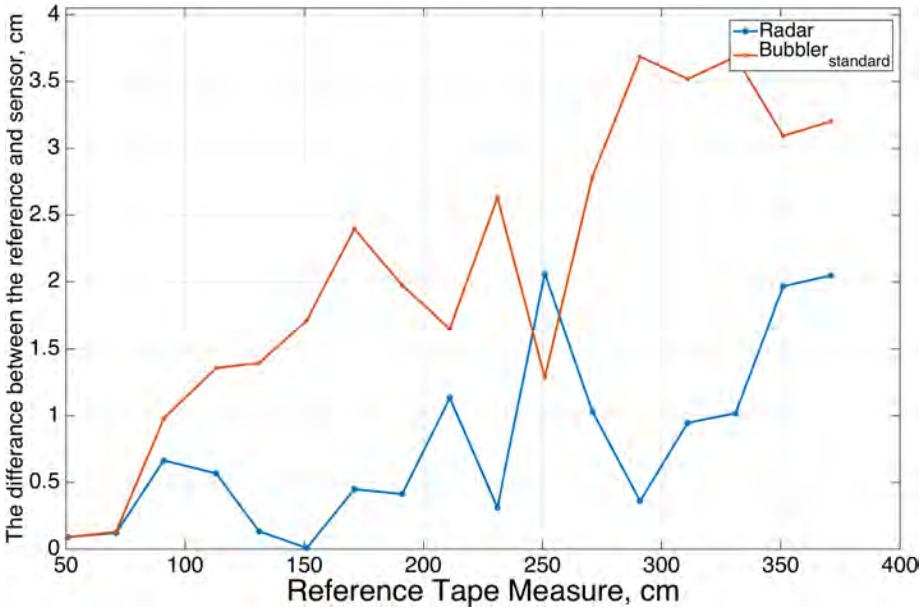

Figure 5.22: The deviation from the reference for the first experiment.

5.6.2 The second experiment, December 2 2014.

Figure 5.24 depicts the mean of each measurement together with the reference as a function of the reference. The next plot, Figure 5.25 show the difference between each sensor and the reference. Since the reference is a tape measure which like the radar measure the distance from a reference point at the top of the well down to the water surface the first point of the sensor data is adjusted to fit perfectly on the reference. Figure 5.26 show the deviation from the mean of each measured level. The trend gets weaker with the water level and at a point change direction. This effect is caused by water leaking into the well through one of the pipes connection the well with the sea. When the water level passes the height of the pipe the flow change direction. This is the cause to the relatively high standard deviations in Table 5.9 and can also explain the deviations in Figure 5.25. The mean used to determine the water surface position is in this case just the mean position of the water surface during the measurement due to the leaking water. A better value to be used would be the first one in the time series. One way to deal with this is to calculate the theoretical position of the water surface as we did in the indoor experiments. Another way would be to redo the experiment and make sure there are no leakage of water into the well. If the trend of each level measurement is subtracted from the data set we get the standard deviations shown in Table 5.10. The data are plotted in Figure 5.27.

Table 5.9: The standard deviation per level from the second experiment.

Level/Sensor	1 (cm)	2 (cm)	3 (cm)	4 (cm)	5 (cm)	6 (cm)	7 (cm)	8 (cm)
Bubbler$_{usgs1}$	0.45	0.287	0.37	0.241	0.148	0.088	0.433	1.094
Bubbler$_{usgs2}$	0.457	0.286	0.373	0.271	0.157	0.085	0.394	1.101
Bubbler$_{usgs3}$	0.451	0.284	0.352	0.27	0.165	0.054	0.418	1.073
Bubbler$_{standard}$	0.463	0.293	0.294	0.197	0.174	0.047	0.427	1.099
Radar	0.422	0.341	0.297	0.202	0.134	0.077	0.389	1.023

Table 5.10: The sensor standard deviation of the de-trended data per level.

Level/Sensor	1 (cm)	2 (cm)	3 (cm)	4 (cm)	5 (cm)	6 (cm)	7 (cm)	8 (cm)
Bubbler$_{usgs1}$	0.04	0.042	0.1	0.081	0.045	0.071	0.054	0.019
Bubbler$_{usgs2}$	0.037	0.041	0.118	0.093	0.05	0.058	0.04	0.032
Bubbler$_{usgs3}$	0.036	0.031	0.099	0.113	0.047	0.034	0.034	0.035
Bubbler$_{normal}$	0.045	0.041	0.039	0.015	0.052	0.035	0.041	0.098
Radar	0.057	0.053	0.052	0.059	0.07	0.062	0.074	0.086

Figure 5.23: The tape measure carrier used in the second experiment.

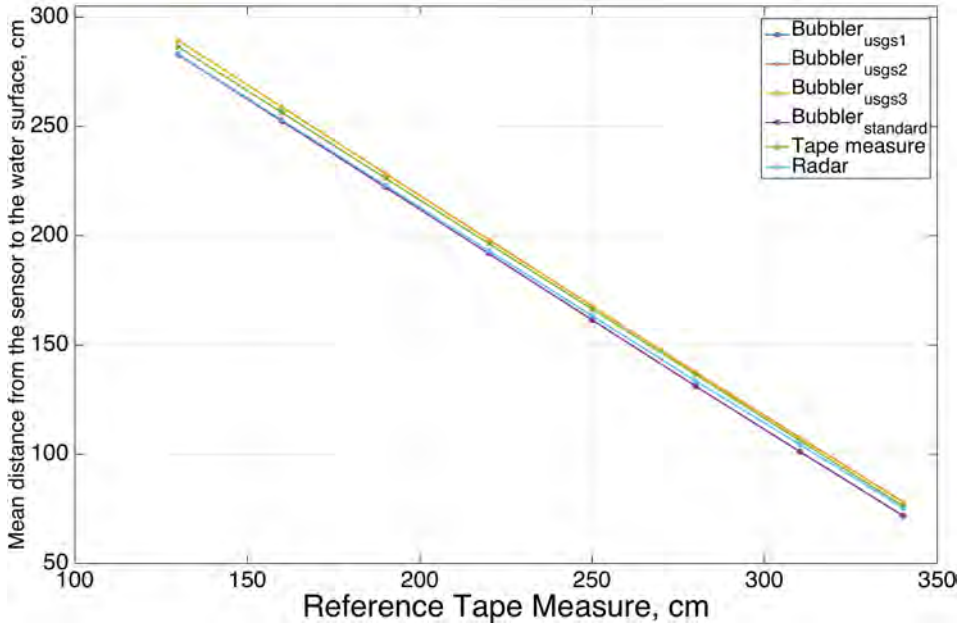

Figure 5.24: The mean for each level together with the reference tape measure.

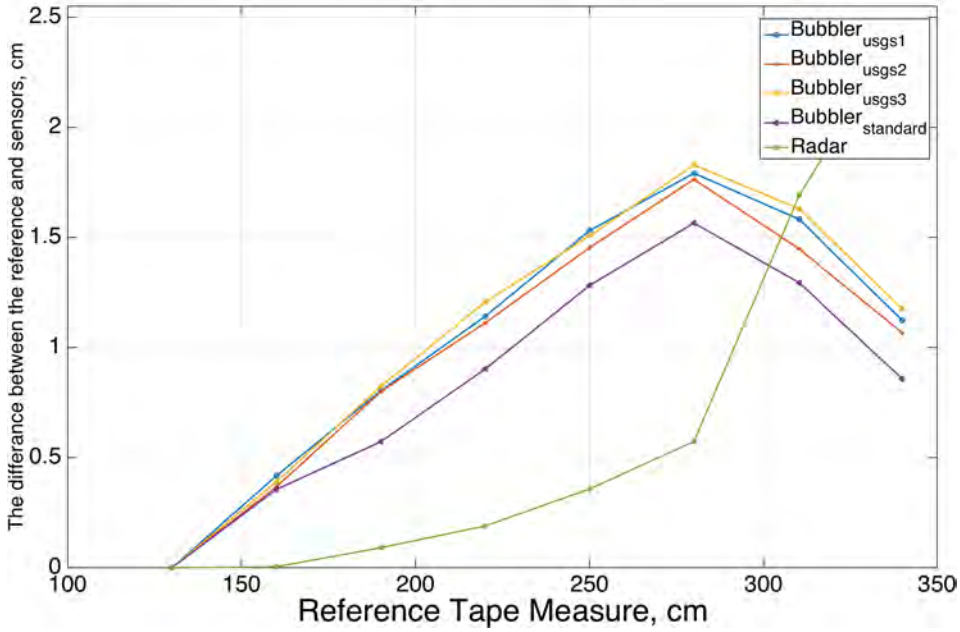

Figure 5.25: The deviation from the reference for the second experiment.

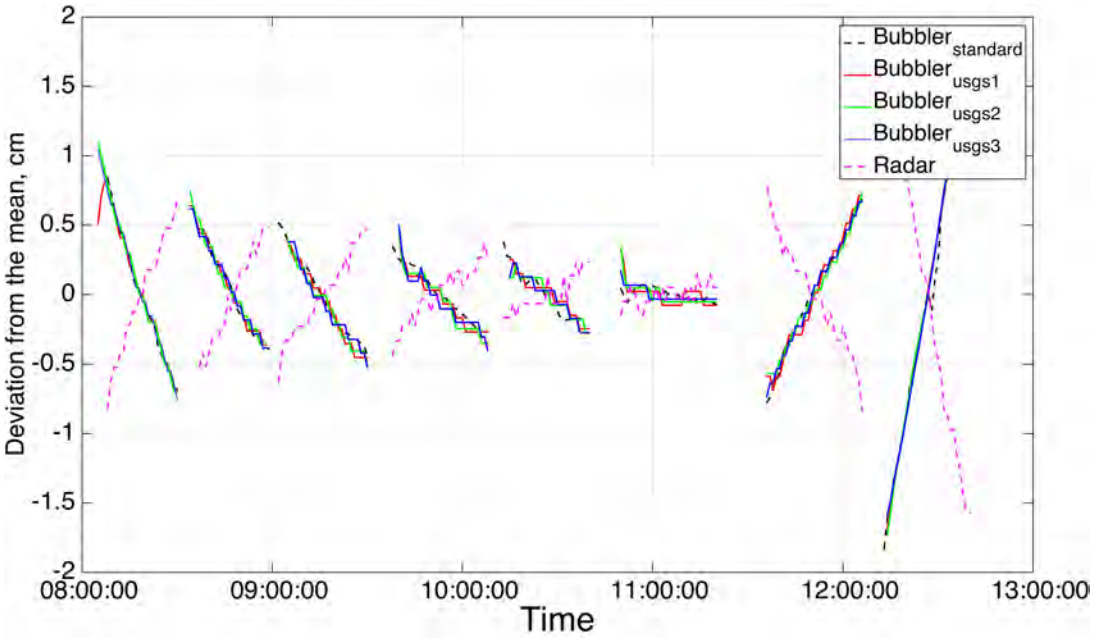

Figure 5.26: The data from from the linearity test divided into levels

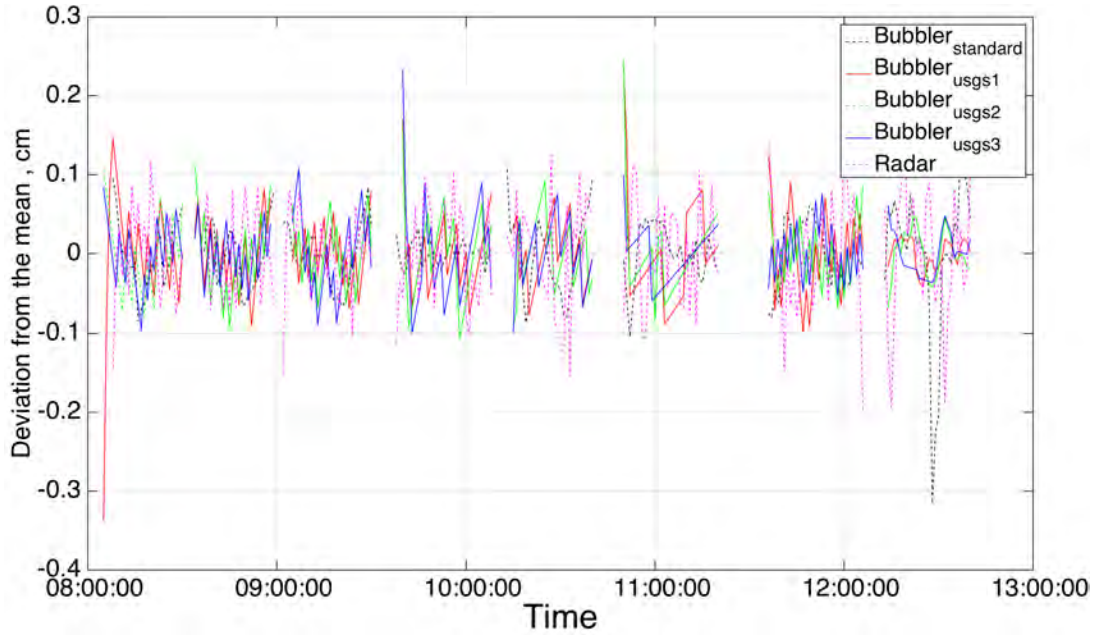

Figure 5.27: The data set in Figure 5.26 with the trends subtracted.

5.7 Wind impact on the measurement error

Figure 5.28: The measurement well during the build up of the storm on January 10.

The bubble sensors are enclosed in a measurement well made out of concrete and embedded in the coastline. This should make an excellent protection from wind and waves. How are the measurements affected by wind? And how do they differ from the unprotected sensor? We will use the error as a measure. Defined as the difference between the radar and each of the bubble sensors. December and January were rather windy with measured wind speeds up to 30 m/s (See Figure 5.29). Figure 5.30 show the distribution of the wind speed. If we look at how the wind speed affect the error we use the radar as reference and look at the differences between the reference and the $bubbler_{usgs1}$, $bubbler_{standard}$ and $bubbler_{outside}$. One would assume the bubble sensor outside the well to be more affected by strong winds than the bubble units in the well. However judging by the graphs there is no strong evidence that this is the case. Of course, the overall variations in the error are larger than the other sensors but the effect does not increase more rapidly with the wind speed than the other ones. Figure 5.33 show that even if the error is over all larger than in the other two cases there does not seem to be a strong correlation with the windspeed as in the case with the normal bubble unit. Once again the problem seem to be a timing error. The normal bubble unit is the only one that is perfectly timed with the radar. Figure 5.35 and 5.34 show the windowed standard deviation of the error of each sensor and the radar and each sensor and the sensor outside the well.

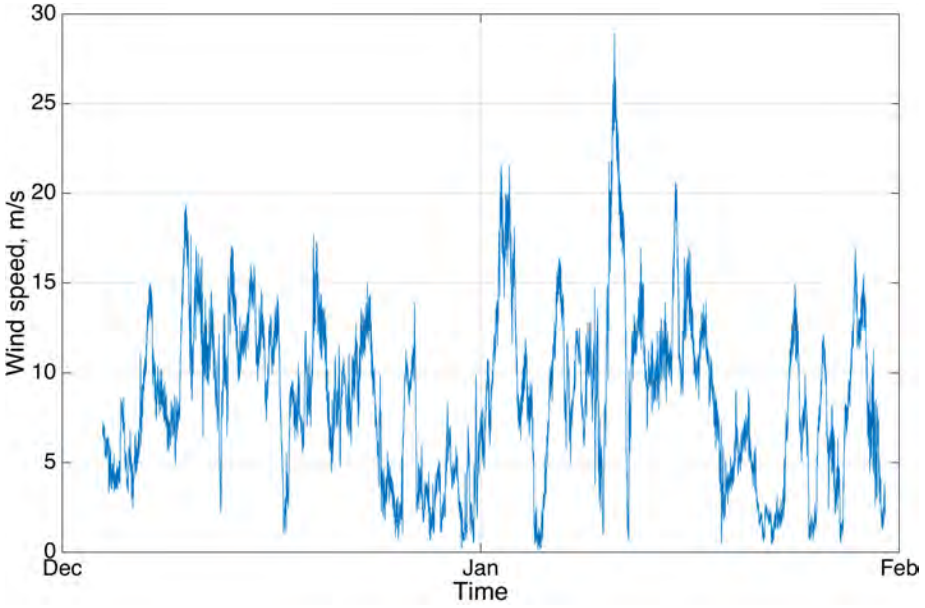

Figure 5.29: The windspeed during December 2014 and January 2015.

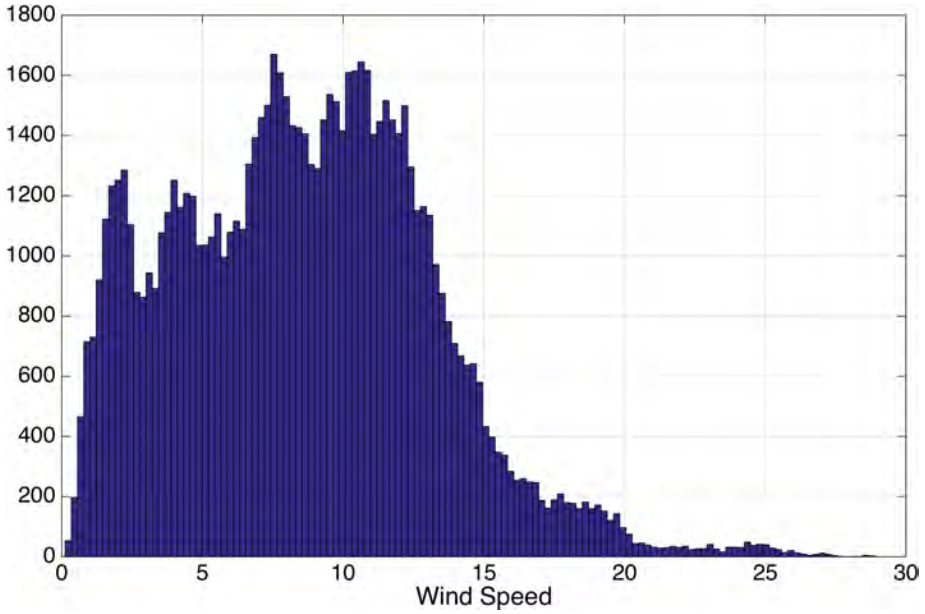

Figure 5.30: The distribution of the wind speed during December 2014 and January 2015.

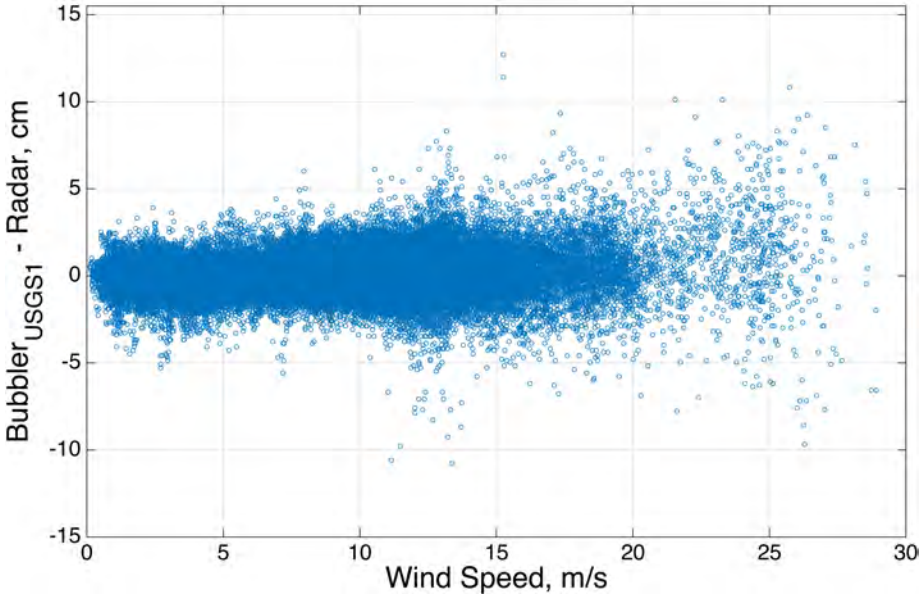

Figure 5.31: The $error = Bubbler_{usgs1} - Radar$ as a function of wind speed.

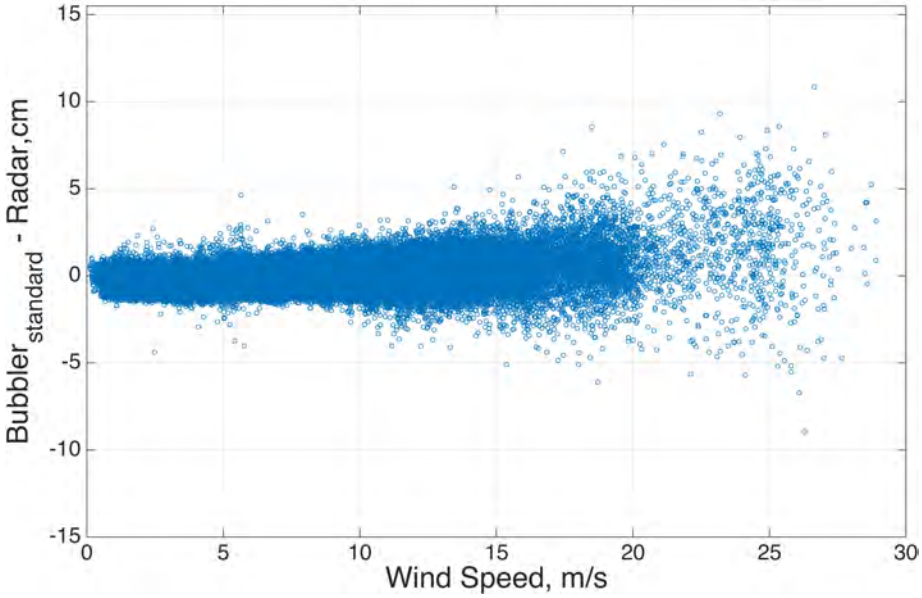

Figure 5.32: The $error = Bubbler_{standard} - Radar$ as a function of wind speed.

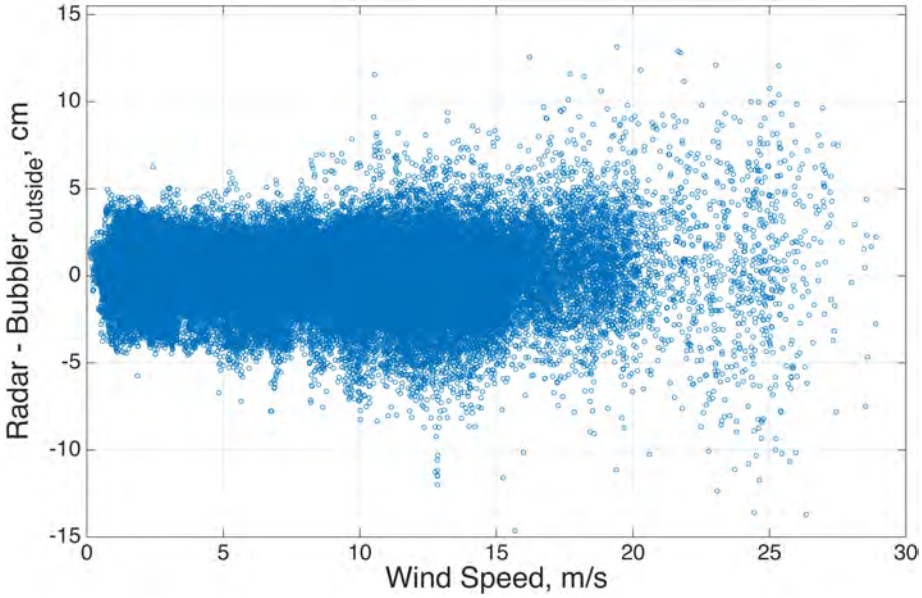

Figure 5.33: The $error = Bubbler_{outside} - Radar$ as a function of wind speed.

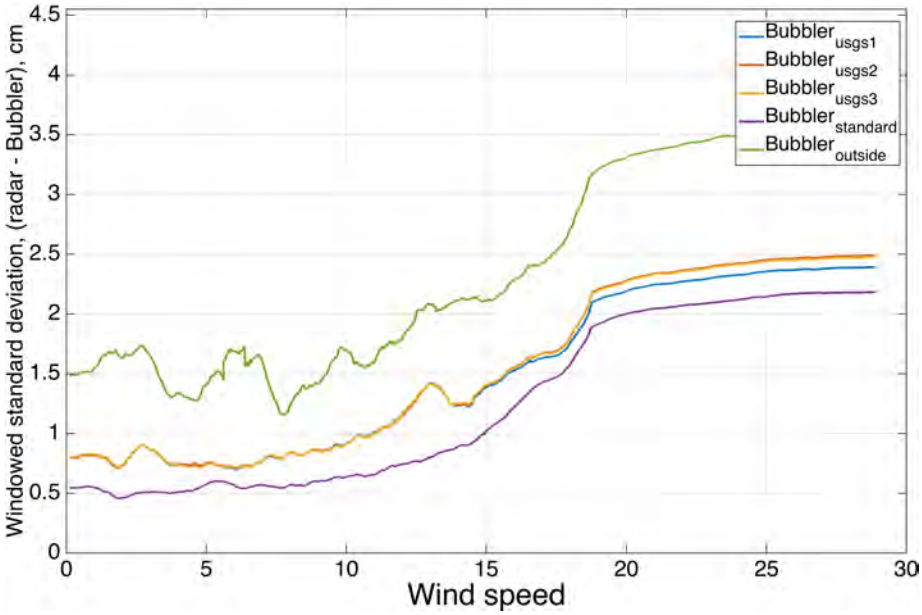

Figure 5.34: The windowed standard deviation of the $error = radar - bubbler$ as a function of wind speed. The window size is 30 minutes.

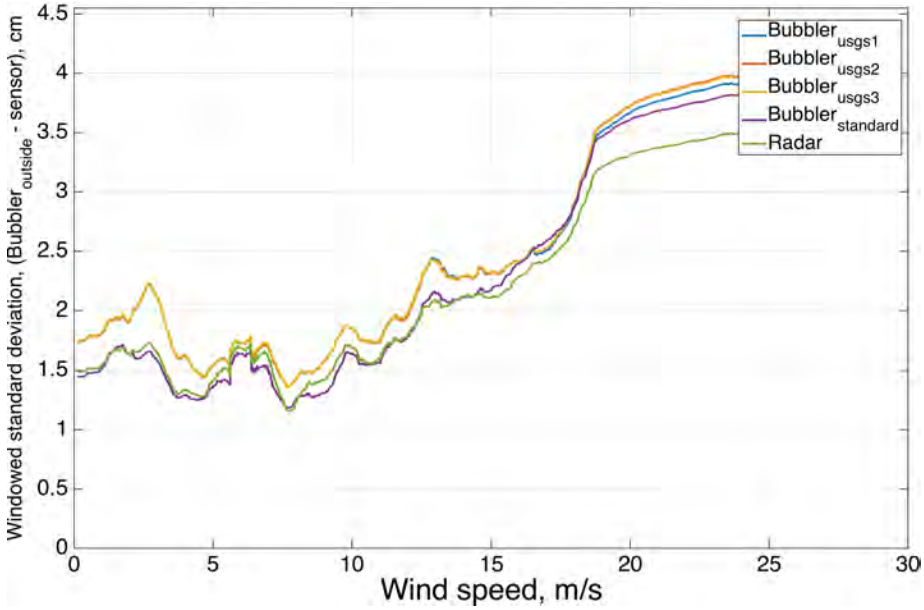

Figure 5.35: The windowed standard deviation of the $error = Bubbler_{outside} - sensor$ as a function of wind speed.The window size is 30 minutes.

Chapter 6

Conclusion

The ability to measure the local sea level with high accuracy is important when investigating the future impact of a global sea level rise. In this report a new tide gauge, currently under construction at the Onsala Space Observatory has been evaluated both in laboratory experiments and in field experiments. The laboratory experiments were performed mostly during the spring and summer 2014 and indicated that placing the radar unit in a too narrow tube could affect the measurements in unexpected ways. A sine formed signal with a peak-to-peak amplitude of 4 mm was superimposed on the measurements. Probably due to reflections in the tube walls but further investigation is required to fully understand the effect. A similar effect could be seen in the field experiments were the Van de Casteele diagram of the radar and the standard bubble sensor show systematic errors in the form of a sinus shaped signal when the water level reach down to about $h_{rad} = 250$ cm. The reason could be reflections in the walls leading to interference of the radar signal. Also in this case, more measurements needs to be done to understand the origin of the effect. The four bubble sensors in the well and the one outside the well show systematic errors in the form of a scale error which is believed to be removed if the salinity level is known. Since the raw pressure data are available old data can be corrected using the actual salinity value. The linearity of the sensors was also investigated. The deviation from the reference became up to 1.7 cm for most of the bubble sensors while the radar showed a better linearity with a deviation of about 0.5 cm. We expect the salinity levels to be the cause of the deviation for the bubble sensors. The radar is however not affected by the water density and the reason for the deviation in this case is unknown. The reference which was a tape measure fastened to a styrofoam buoy is suspected to be non-linear as well. The stilling well has as its prime mission to function as a low pass filter of the sea surface and to keep the surface free from ice. There are three pipes in the well which let sea water flow in and out of the well and the diameter of the pipes will affect the low pass characteristic of the tide gauge. The measurements showed that the error, as expected, grew with the wind speed and suggested that the pipes can be narrowed for better performance. However one could also filter the high frequency components with software. The latter would give more options but requires a fast enough sampling frequency.

Chapter 7

Future work

As a first step to improve the accuracy of the measurements the timing of the bubble sensors should be adjusted. They measure at slightly different times and therefore the analysis of the measurements are made harder. To further improve the measurement accuracy it is suggested that the salinity level is measured and that the bubble sensors are adjusted accordingly. It is even possible to continuously update the salinity levels via the remote interface if such data were available. To improve the radar measurement accuracy it is recommended that the systematic errors of the radar are investigated more thoroughly by using a better reference measure and making sure there are no leakage into or out of the well.

Bibliography

Douglas B, Global Sea Level Rise, Journal of Geophysical Research, Volume 96, Issue C4 , pp 6981 - 6992. 1991, ISSN 0148-0227

Jacobson, M.D., Hogg D.C., & Snider J.B., Wet Reflectors in Millimeter-Wave Radiometry-Experiment and Theory *IEEE Trans. Geosci. Rem. Sens.* **GE-24**, 5. pp. 784-791, September 1986.

Löfgren, J S. Local Sea Level Observations Using Reflected GNSS Signals , **ISBN:978-91-7385-955-4**,*Department of Earth and Space Sciences Space Geodesy and Geodynamics Chalmers University of Technology*, 2014

Manual on Sea-level Measurements and Interpretation, Volume IV : An update to 2006, Paris, Intergovernmental Oceanographic Commission of UNESCO. 78 pp. (IOC Manuals and Guides No.14, vol. IV ; JCOMM Technical Report No.31; WMO/TD. No. 1339) (English) Available at: http://www.psmsl.org/train_and_info/training/manuals/ . Accessed 28 July 2014.

McCutcheon, S.C., Martin, J.L, Barnwell, T.O. Jr. 1993. Water Quality in Maidment, D.R. (Editor). Handbook of Hydrology,McGraw-Hill, New York, NY (p. 11.3)

Overpeck. Jonathan T. , Bette L. Otto-Bliesner, Gifford H. Miller, Daniel R. Muhs, Richard B. Alley, Jeffrey T. Kiehl,Paleoclimatic Evidence for Future Ice-Sheet Instability and Rapid Sea-Level Rise. SCIENCE VOL 311 24 MARCH 2006

Solomon S,Plattner G K, Knutti R & Friedlingstein P 2009 Irreversible climate change due to carbon dioxide emissions Proc. Natl Acad. Sci. 106 1704

Stoew, B., C. Rieck, and G. Elgered, First results from a new dual-channel water vapor radiometer, *Proc. of the 14th Working Meeting on European VLBI for Geodesy and Astrometry*, Castel San Pietro Terme, 8–9 September, 2000, edited by P. Tomasi, F. Mantovani, and M. Perez Torres, pp. 79–82, 2000.

Strauss B, Ziemlinski R, Weiss J & Overpeck J T, Tidally-adjusted estimates of topographic vulnerability to sea level rise and flooding for the contiguous United States Environ. Res. Lett. 2012

Uno, Paul., Plastic Shrinkage and Evaporating Formula, *ACI Materials Journal, American Concrete Institute.*, Julyugust 1998.

Vellinga P, Katsman C A, Sterl A and Beersma J J 2009 Exploring high-end climate change scenarios for flood protection of the Netherlands International Scientific Assessment Carried out at the Request of the Delta Committee (De Bilt: KNMI)

Olav Vest, Determination of Postglacial Land Uplift in Fennoscandia from Leveling, Tide-gauges and Continuous GPS Stations using Least Squares Collocation, Journal of Geodesy, Volume 80, Issue 5 , pp 248-258. 2006

Appendix A

Mobrey Series 9700, hydrostatic level transmitter

Instruction Leaflet
IP342, Rev. AB
November 2007

Mobrey Series 9700

Hydrostatic level transmitter

Features

- Loop powered
- 4 to 20mA output
- Intrinsically safe option
- +/- 0.1% accuracy
- 10:1 rangeability
- Spans from 0.2 to 200 m H_20
- Integral or remote calibration
- Good long-term stability
- Ceramic capacitive sensor
- Wide range of process connections
- Direct process mounting
- Approved by the world's leading Marine Classification societies

The 9700 Hydrostatic Level Transmitter is a measuring instrument and should be handled with due care and attention at all times.

- Do not swing sensor by the cable
- Do not drop or impact the sensor

Contents

Section 1 : Specification

Functional

	9710, 9720, 9780 Suspended in tank	9790 External to tank
Output signal : Power supply : Load resistance : Measuring ranges :	Two-wire, 4-20mA 10-30V d.c. R = 50 x (supply voltage -10V) Ω Up to 200m / 8" to 656ft H_20	Two-wire, 4-20mA 10 - 30V d.c. R = 50 x (supply voltage -10V)Ω Up to 200m / 8" to 656ft H_20
Overrange limit :	Max 600m / 1968ft H_20	Max 600m / 1968ft H_20
Span adjustments : Process temp. limits : (non certified)	+10 to 100% URL* -20 to + 60°C / -4 to +140°F	+10 to 100% URL* -20 to + 90°C (80°C Ex ia)
Ambient temp. limits : Humidity limits :	-20 to + 90°C (-20 to +80°C Ex ia) 0 to 100% RH	-20 to + 90°C (-20 to +80°C Ex ia) 0 to 100% RH
Hazardous area use : Cable specification :	ATEX II 1 G EEx ia IIB T4 CSA (Canada & USA) Capacitance 500 pF/metre Refer to Section 4	ATEX II 1 G EEx ia IIB T4 CSA (Canada & USA) Capacitance 500p F/metre Refer to Section 4

Performance

	9710, 9720, 9780 Suspended in tank	9790 External to tank
Accuracy : Stability : Temperature effect : Response time :	+/- 0.1% (BSL)** of calibrated span +/- 0.1% URL* per 6 months +/- 0.015% URL per °C See Section 5.5	+/- 0.1% (BSL)** of calibrated span +/- 0.1% URL* per 6 months +/- 0.015% URL per °C See Section 5.5

Physical

	9710, 9720, 9780 Suspended in tank	9790 External to tank
Process connection :	Submersible	Flange mounted
Wetted Parts : Sensor : Sensor Housing : Sensor 'O' Rings :	 Ceramic 316 St. Steel or Aluminium Bronze Fluorocarbon (FPM/FKM) Nitrile	 Ceramic 316 St. Steel or Aluminium Bronze Fluorocarbon (FPM/FKM) Nitrile
Body 'O' Rings	Fluorocarbon (FPM/FKM) or Nitrile	Fluorocarbon (FPM/FKM) or Nitrile
Cable Seals	Fluorocarbon (FPM/FKM) or Nitrile	Fluorocarbon (FPM/FKM) or Nitrile
Cable :	Polyurethane or FEP coated	Polyurethane or FEP coated
Pole :	316 Stainless steel pole supplied with 316 Stainless steel housing option. Copper Nickel pole supplied Aluminium Bronze Housing option	Not applicable
Ingress Protection : Approximate weight :	IP68 / NEMA 6P (200m / 656ft H_20) 0.7Kg / 1.54lbs (sensor only)	IP68 / NEMA 6P (200m / 656ft H_20) 0.7Kg / 1.54lbs (sensor only)

** URL = Upper range limit* *** BSL = Best straight line, includes effects of linearity, hysteresis & repeatability*

Remote Enclosures

Remote enclosure :	Aluminium IP67 Grey (RAL 7001) 0.7 kg
Bellows enclosure :	Polyester IP67 Grey (RAL 7001) 1.2 kg

Appendix B

OTT Compact bubbler system, specifications

Water level measurement
OTT CBS – compact bubble sensor
for measuring depth and water level

OTT CBS

Indirect measurement principle for precise data

The OTT Compact Bubble Sensor (CBS) measures water levels accurately and remains stable long-term. It operates according to a non-drifting measurement principle, covering a range of measurement of up to 30 m. The system uses an indirect measurement technique that keeps the pressure measurement cell and electronics out of the water.

An integrated compact piston pump produces the bubbling pressure required for the indirect measurement process. The compressed air is blown out in the water with the attached measuring tube using a bubble chamber – after the blowing process the pressure between the measuring tube and the water pressure at the bubble chamber is equalized. A pressure measuring cell in the OTT CBS measures the air pressure and the prevailing tube pressure in succession. By taking the difference between both signals, the exact water level is calculated compensated for drift.

By using an intelligent pumping strategy, the bubble sensor doses the exact amount of air required in order to be able to guarantee a precise water level measurement and minimize condensation. In addition, power consumption is reduced and the lifetime of the pump unit increased.

Quantitative
Hydrology

OTT CBS – accurate, compact, and reliable

Features and Benefits

— Optimized pump strategy for low power consumption and high dynamics (1 m level change/minute can be detected)
— Integrated overload protection – continual monitoring of the tube pressure and the motor current of the pump
— No software needed for initial startup – all settings are made via DIP switches
— Simple system integration into existing networks and stations – SDI-12 interface and scaleable 4...20 mA output present
— Air inlet with dust protection – no air drying needed in the 15 m measuring range
— Connection of measuring tubes with different inner diameters of 2 mm, 4 mm or 1/8" possible; existing 4 mm standard pneumatic measuring tubes can also be used.

Quickly and easily mounted

Individually tailored

— Optional: An advanced version with an extended calibration and air drying unit allows measurements of up to 30 m – particularly suitable for applications at dams or water reservoirs.
— Optional: For special applications a version with ±3 mm accuracy in the first 4.5 m of the 15 m range is available (USGS Specification).

DIP switches for easy programming

Applications

— Water level measurement in streams, rivers, canals, lakes
— Dams, irrigation plants, water reservoirs
— Garbage depots, industrial and mining waste water
— Channels with long, flat embankments
— Especially suitable for areas prone to lightning strikes (indirect measurement principle)

Accessory: OTT EPS 50 bubble chamber

Technical data

Sensor Technology
Bubble sensor,
indirect pressure measurement

Measuring ranges
- Standard version + USGS Specification: 0 … 15 m (0… 50 ft)
- Measuring range 30 m version: 0 … 30 m (0… 100 ft)

Resolution
1 mm (0.01 ft)

Accuracy
- Standard version + Measuring range 30 m version: ±5 mm
- USGS Specification version*: measuring range 0 … 15 ft: ±0.01 ft; measuring range 15 … 50 ft: ±0.065 % of measured value or ±0.02 ft, whichever is less

Measuring dynamics (max. level change)
1 m/min

Units
m, cm, ft, mbar, psi

Interfaces
4 … 20 mA, SDI-12, SDI-12 via RS-485

Power supply
9.6 ... 30 V DC, typ. 12/24 V DC

Power consumption
- Sample interval 1 min: typ. 320 mAh/day
- Sample interval 15 min: typ. 25 mAh/day

Measuring tube
Inner diameter typ. 2 or 4 mm

Dimensions
165 mm x 205 mm x 115 mm

Weight
approx. 1500 g

Housing material
ABS

Protection type
IP 43

Temperature range
- Operational: –20 … +60 °C
- Storage: –40 … +85 °C

Relative humidity
10 … 95 % non-condensing

EMC limits
IEC61326 and EN61326 are adhered to

CE

Order numbers
- OTT CBS: 63.200.001.9.2
- Coding Standard: 1
- Coding USGS-Specification: 2
- Coding Measuring range 30 m: 3

*The OTT CBS with increased accuracy requires regular calibration.

Hydromet
Germany
OTT Hydromet GmbH
Ludwigstrasse 16 · 87437 Kempten
Phone +49 831 5617-0 · Fax -209
info@ott.com · www.ott.com

Appendix C

CS476 Radar, specifications

6. Specifications

Features:

- FCC compliant
- Ideal for areas where submersed sensors can be damaged due to corrosion, contamination, flood-related debris, lightning, or vandalism
- Compatible with most Campbell Scientific dataloggers (including the CR200(X) series)
- Low maintenance—no moving parts significantly reduces maintenance cost and time
- Low power consumption
- Rugged enough for harsh environments—NEMA rated 4X
- Individual FCC license not required

Compatibility

Dataloggers: CR200(X) series
CR800 series
CR1000
CR3000
CR5000
CR500
CR510
CR10(X)
CR23X

Measurement Range (see FIGURE 6-1)

CS475: 50 mm to 20 m (2 in to 65 ft)
CS476: 50 mm to 30 m (2 in to 98 ft)
CS477: 400 mm to 70 m (16 in to 230 ft)

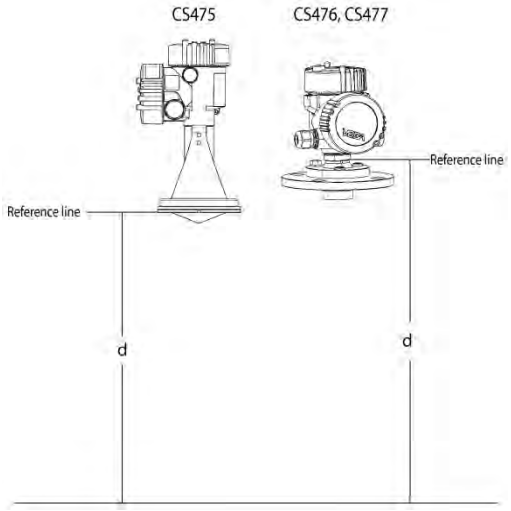

FIGURE 6-1. Reference line for measurement range

Accuracy
- **CS475:** ±5 mm (±0.2 in)
- **CS476:** ±3 mm (±0.1 in)
- **CS477:** ±15 mm (±0.6 in)

Resolution: 1 mm (0.0033 ft)

Output Protocol: SDI-12

6.1 Radar Unit

Frequency: ~26 GHz

Electromagnetic Compatibility: Emission to EN 61326; Electrical Equipment Class B

Pulse Energy: 1 mW maximum

Beam Angle
- **CS475:** 10° (3-in dia horn)
- **CS476, CS477:** 8° (4-in dia horn)

Power Requirements
- **Input Voltage:** 9.6 to 16 Vdc
- **Surge Protection:** 1.5 KVA

Typical Current Drain with 12 V Power Supply
- **Sleeps:** 4.7 mA
- **Measurement:** 14 mA

6.2 Environmental

Operating Temperature Range: –40° to +80°C

Storage Ranges
- **Temperature:** –40° to +80°C
- **Relative Humidity:** 20% to 80% RH

Temperature Sensitivity: average TK: 2 mm/10 K, max 5 mm over the entire temperature range of –40°to +80°C

Vibration Resistance: Mechanical vibrations with 4 g and 5 to 100 Hz

6.3 Physical

See FIGURE 6-2 and FIGURE 6-3 for dimensions.

Rating: NEMA 4x

Housing Material: Aluminum, coated IP66/68

Horn Material: 316L stainless steel

Weight

CS475: 2 kg (4 lb)

CS476/CS477: 4.3 kg (9.4 lb)

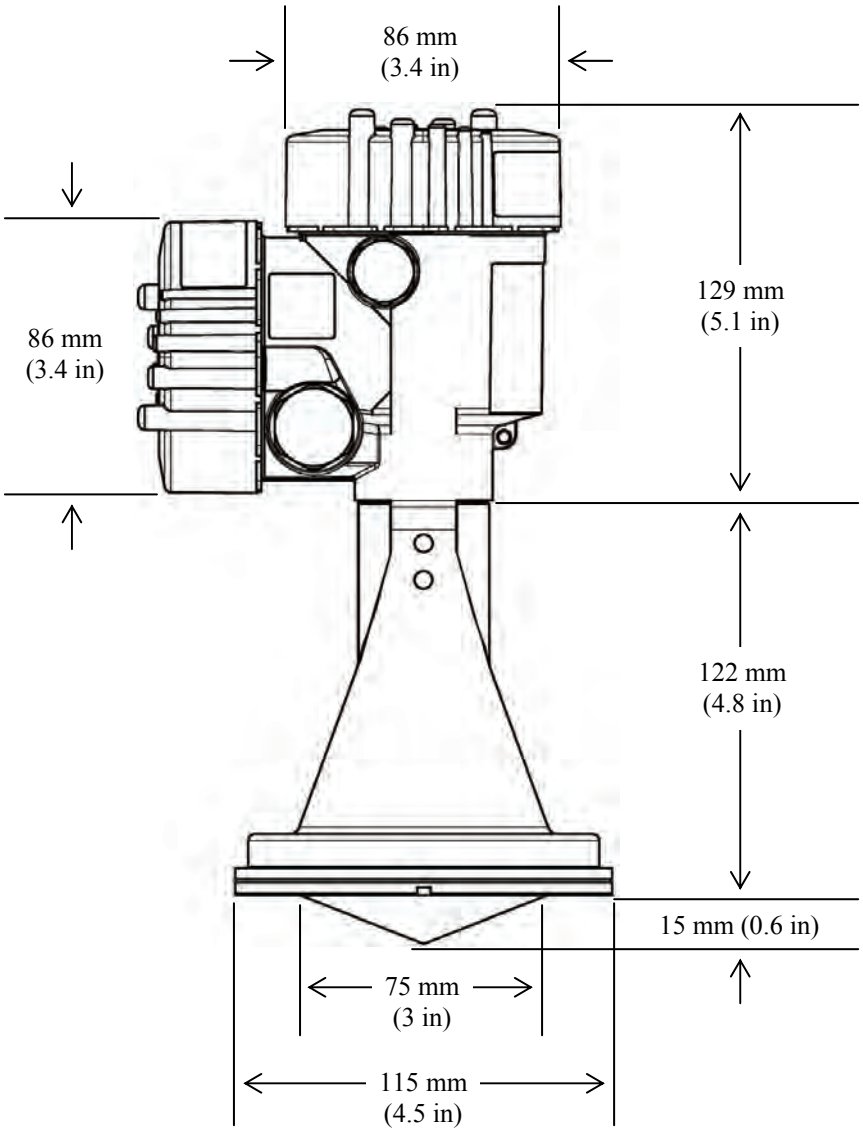

FIGURE 6-2. CS475 dimensions

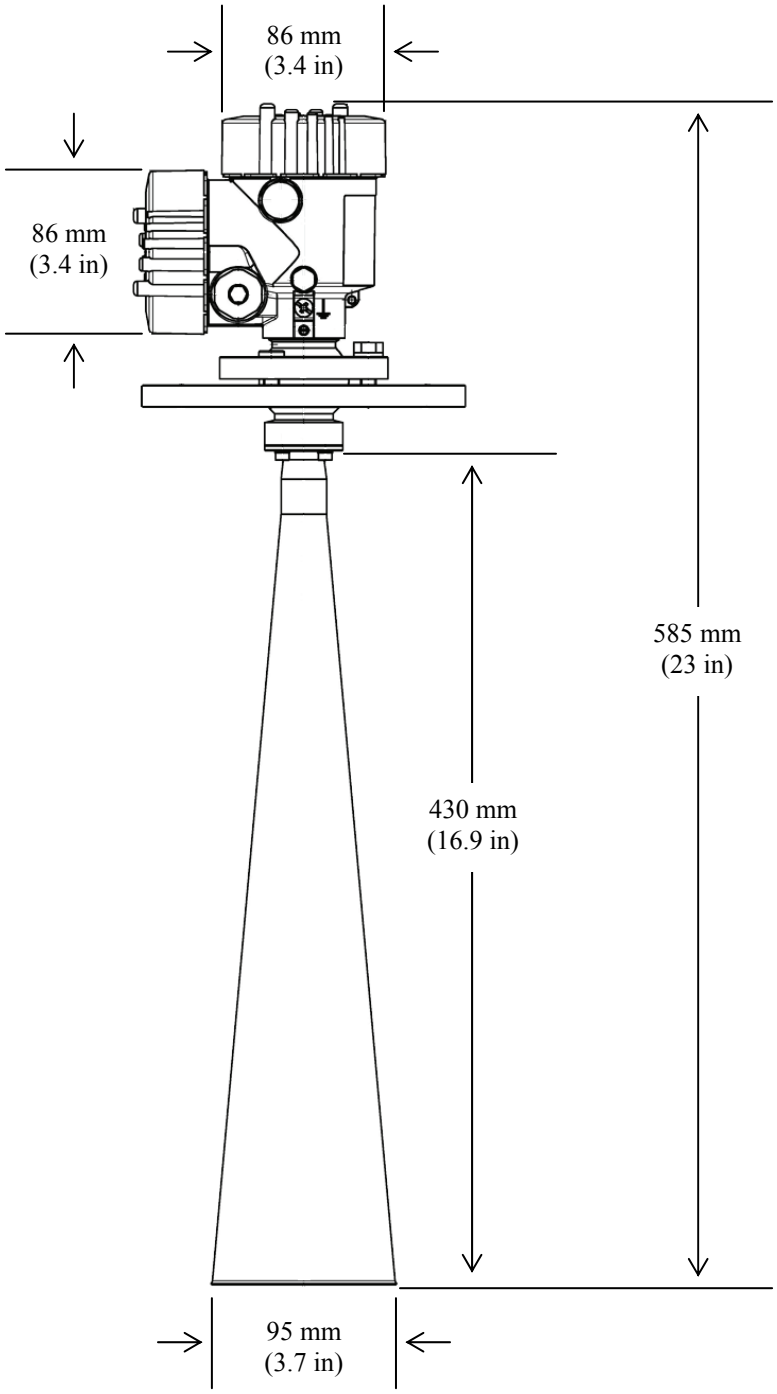

FIGURE 6-3. CS476/CS477 dimensions

Appendix D

ADAM sampling unit, specifications

ADAM-6000 Series

Features

- Ethernet-based smart I/O
- Mixed I/O in single module
- Pre-built HTTP server and web page in each module for data/ alarm monitoring
- User-defined web pages
- Active alarm/event trigger handling
- Industrial Modbus/TCP protocol
- Remote F/W upgrade through the internet
- Pre-built mathematic functions in analog input modules
- ADAM.Net Class Library software support

The Path to Seamless Integration

The integration of automation and enterprise systems require a change in the architecture of open control systems. From Advantech's point of view, the level of integration between automation and enterprise systems can only be accomplished through Internet technology. The seamless level of integration between plant floor and office floor has not been achieved in all automation systems. However, many enterprises are approaching this goal.

The key element of the seamless integration is a common network architecture, which breaks the traditional layers (enterprise layer, plant information layer, control layer and device level layer, sensor layer) that require a data gateway as an interface to communicate between different layers. Industrial Ethernet is regarded as the most appropriate network to accomplish the task in industrial automation.

It is believed that IP/Ethernet protocols will progress beyond the control layer, into the field layers. Placing remote I/O with IP/Ethernet connections on the shop floor is economical. Advantech believes that over the next five years, Internet protocols over Ethernet will dominate major field connections. The Advantech ADAM-6000 series comprises industrial-grade Ethernet hubs/switches/fiber optics for infrastructure Ethernet solutions in industrial automation environments.

Control Strategy Moves to Field Devices

It is a trend to move I/O to remote locations to reduce wiring costs. Remote I/O is becoming smarter and equipped with control functions as they move from today's 16 to 64 I/O multi-plexers to the smallest remote I/O units, with perhaps as few as four I/O in the near future.

The ADAM-6000 series is designed to realize the concept of the smart I/O blocks. With control algorithms and mathematical functions built in, the ADAM-6000 series is a revolutionary smart I/O module close to the sensor layer in automation.

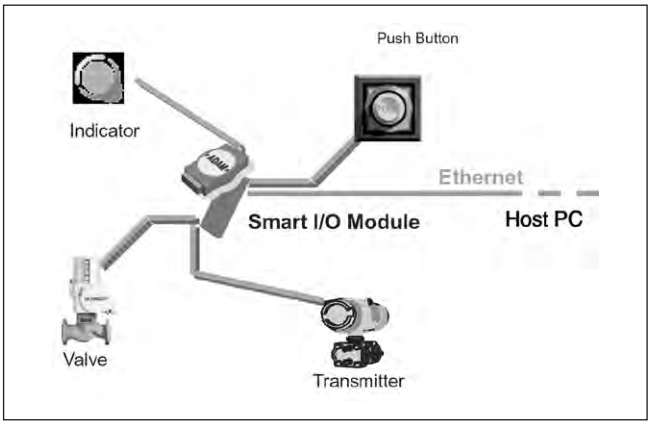

The Future Concept of Smart I/O Blocks

Web-enabled Technology Becomes Popular on Factory Floors

As Internet technologies and standards have rapidly developed over the past decade, Web-based control methodologies now obviously represent a powerful opportunity for extending efficient network-based management techniques to encompass non-IT real-world assets.

The ADAM-6000 series is equipped with a built-in web server so that its data can be viewed, anytime-anywhere via the Internet. Moreover, ADAM-6000 allows users to configure user-defined web pages to meet the diverse needs in various applications. With this powerful function, the ADAM-6000 series breaks the boundary of traditional multi-layer automation architecture and allows users to access field data directly in real time, which enables seamless integration between the plant floor and the front office.

HMI has provided a friendly operator interface for discrete control and sharply reduced the cost and complexity of automation systems. A web server has been added to most HMI software and a browser allows access to HMI displays from remote locations via the network. The end user is able to see and use an identical HMI from any Internet connected computer anytime, anywhere. ADAM-6000 can be be fully integrated with standard HMI software which supports Modbus TCP/IP, including Advantech Studio.

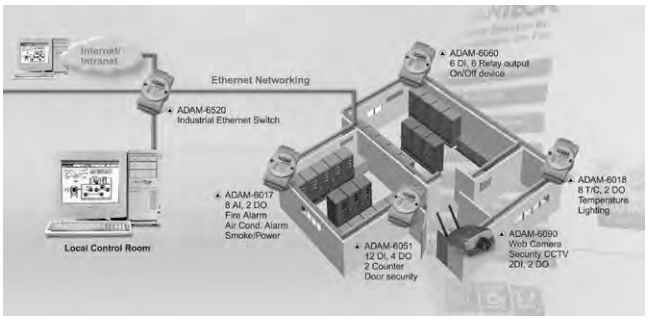

ADAM-6000 Application Architecture

ADAM-6000 Smart Web Ethernet I/O

The integration of automation and enterprise systems and the adoption of an e-manufacturing strategy requires a shift in the manufacturing system architecture. E-manufacturing demands open access to real-time production data from the field. To achieve a seamless level of integration between plant floors and the enterprise level, some fundamental changes have to occur in I/O systems. E-manufacturing means the power of the Internet and I/O systems are used to take things one step further by leveraging Internet technology. These revolutionary I/O systems are web-enabled, smart and are "just-fit" mixed I/O modules. Improvement of the PLC has been gradually moving from logic and I/O in a single chassis, to I/Os in remote locations. The ADAM-6000 series is based on the concept described above.

Why Smart I/O ?

To meet the requirements of future automation, smart I/O blocks have become popular in I/O system design. To implement the smart I/O blocks concept, I/O systems should be placed as close to the field sensors as possible. Therefore, intelligent control algorithms or basic mathematical functions are essential in I/O systems. ADAM-6000 provides intelligent functions that accelerate future automation development.

Why Web I/O ?

The Internet is the major technology that allows all levels of an organization to be able to communicate and make the sensor-to-boardroom model a reality. Access can be realized from any device that utilizes a standard web browser, so connections between remote manufacturing plants, production planners, plant managers, and the CEO can be made without having to create a dedicated proprietary network. Since a web page can be installed in the I/O system as a Web I/O, then not only a sensor-to-boardroom model can be practiced, but sensor-to-home, and a sensor-to-mobile display can also be realized. ADAM-6000 Smart Web Ethernet I/O modules provide built-in standard and customizable web pages, which truly demonstrate the power of Web I/O.

Why Mixed I/O ?

The impact of a tailor-made business model is spreading in automation, and I/O design is no exception. Over the past few years, the average size of PLCs have been reduced by the use of many small and micro PLCs to replace larger PLCs. A compact-sized and application-oriented mixed I/O is the trend. A just-fit mixed I/O module reduces the engineering effort, as well as installation and maintenance cost. It simplifies system architecture and increases system reliability. Obviously the ADAM-6000 series is the perfect choice to meet the specific requirements of many vertical markets.

Common Key Features

1.Industrial Ethernet Networking

The ADAM-6000 series provides various communication modules such as Ethernet hubs, Ethernet switches and Ethernet switches with fiber ports. ADAM-6000 supports both Modbus/TCP and UDP. Embedded with a 10/100 Mbps Ethernet chip, ADAM-6000 supports industrial Modbus/TCP over TCP/IP networks which are commonly used in most business environments. ADAM-6000 also supports UDP, which allows users to develop their applications and handle events.

2.Smart and Mixed I/O Modules

ADAM-6000 provides built-in mathematical functions, including MAX, MIN, AVG, and others in analog input/output modules. ADAM-6000's mixed I/O modular design optimizes the performance and usage of I/O and minimizes the engineering efforts and maintenance cost.

3.Built-in Standard and User-defined Web Pages

ADAM-6000 adopts web technology to enable remote monitoring via Internet. In addition to standard web pages, ADAM-6000 allows users to use the Java programming language to develop pages to meet their own requirements. ADAM-6000 supports standard HMI software with Modbus/TCP OPC drivers and ActiveX drivers.

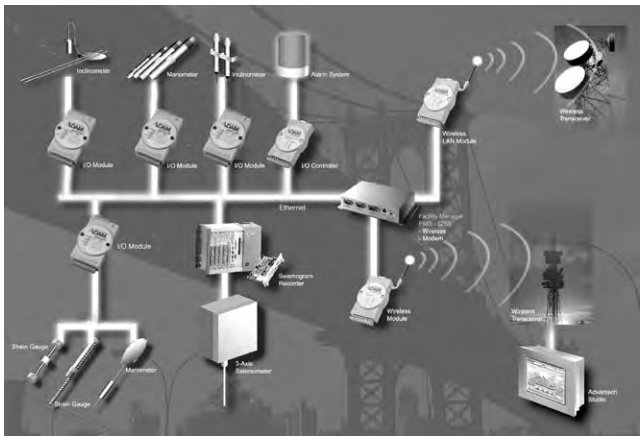

ADAM-6000 Application Diagram

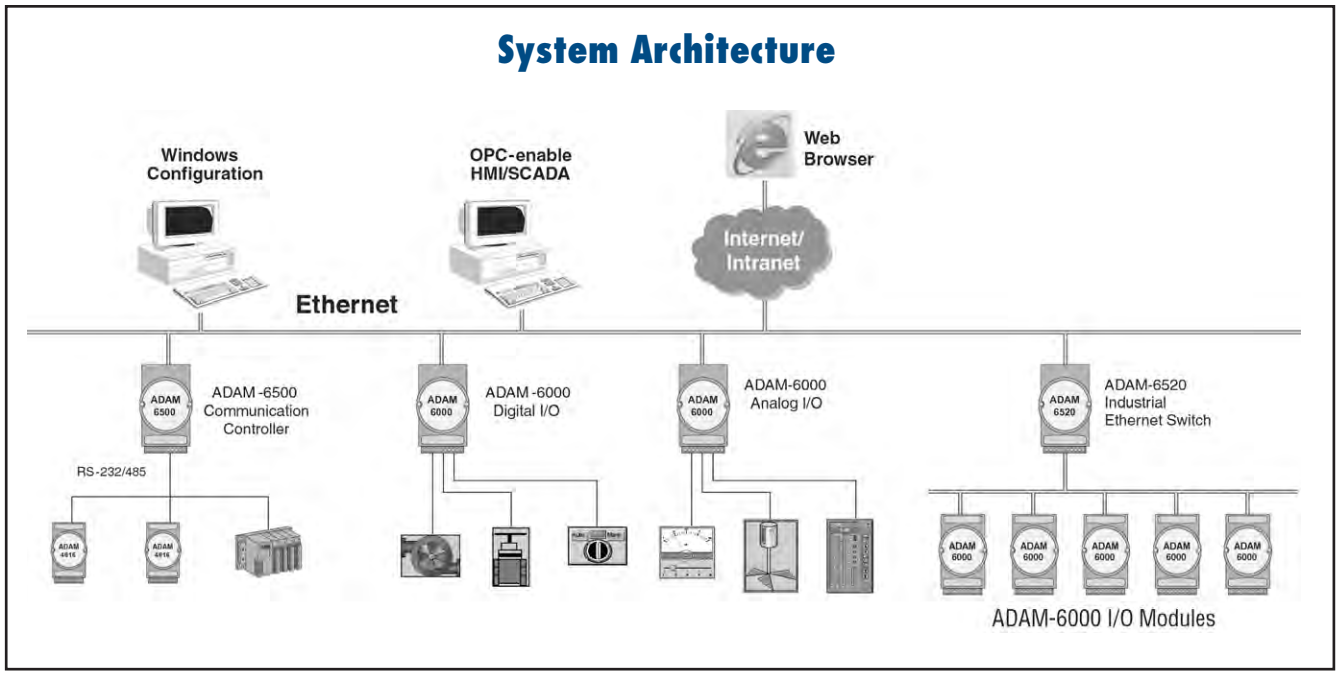

The ADAM-6000 is a controller independent, distributed I/O solution with modular design for maximum flexibility. Its powerful onboard intelligence makes it well suited to SCADA and stand-alone control applications.

Ethernet-enabled Networking

The ADAM-6000 series Ethernet-enabled data acquisition and control module works as an Ethernet I/O data processing center. This new product is not only a standard I/O, but also an intelligent system designed with local control functions and a Modbus/TCP standard for users to easily develop various applications over Ethernet.

Analog Input Modules

The ADAM-6000 analog input modules use microprocessor-controlled, high-resolution, 16-bit, sigma-delta A/D converters to acquire sensor signals such as voltage, current, thermocouple or RTD. They translate analog data into two's complement. After the modules receive a request from the host, they send the data in the desired format over the Ethernet network. ADAM-6000 analog input modules protect your equipment from ground loops by providing 3000 V_{DC} isolation. The ADAM-6017 and ADAM-6018 modules feature digital outputs which may also be used for alarms and event counting. The analog input module's two digital output channels are open-collector transistor switches that you can control from the host computer. By switching solid state relays, the output channels can control heaters, pumps and other power equipment. The module can use its digital input channel to sense the state of a remote digital signal.

Programmable Alarm Output

Analog input modules include high and low alarm signals with remotely configurable boundary values. After each A/D conversion, the digital value is compared with the high and low limit. The module can change the state of a digital output depending on the result of this comparison. This function allows it to perform on/off control of a device independently of the host PC.

Independent Channel Input Type Configuration

The ADAM-6015 6-channel RTD module, provides independent channel input type configuration. You can configure PT-100, Pt-1000 or Balco mA for each channel. This independent channel input type configuration gives the ADAM-6015 more flexibility for versatile applications. This functionality saves customers the cost of buying multiple modules and reduces inventory as well.

Loop Controller Module

The ADAM-6022 offers two analog inputs, two analog outputs, two digital inputs and four digital outputs in one module. The ADAM-6022 is a two loop PID controller. Each loop may be configured as single loop, dual loop ratio, dual loop cascade or single loop with override. An auto tune function is provided to maximize the effectiveness of the control.

Analog Input Modules

The ADAM-6017/6018 are 16-bit, 8-channel analog input modules that provide programmable input ranges on all channels. These modules are an extremely cost-effective solution for industrial measurement and monitoring applications. 3000 V_{DC} optical isolation between the analog input and the modules protects the modules and peripherals from damage due to high input-line voltages.

The ADAM-6018 also supports thermocouple input in combination with the ADAM-6015 7 channels RTD input module. These two modules can offer a complete solution for temperature measurement applications.

Digital Input and Output Modules

The ADAM-6050 features twelve isolated digital input channels and six isolated digital output channels. The outputs are open-collector transistor switches that you can control from the host computer. You can also use the switches to control solid-state relays, which in turn can control heaters, pumps or other power equipment. The host computer can use the module's digital inputs to determine the state of limit switches, safety switches or remote digital signals. The ADAM-6051 provides twelve isolated digital input channels, two isolated digital output channels and two counter channels. All have 5000 V_{RMS} isolation to prevent ground loop effects and prevent damage from power surges on the input lines.

Digital Input

The ADAM-6050 & ADAM-6051 digital input channels provide four operational modes:

- Normal digital input with inverter setting
- 3 kHz frequency
- 3 kHz counter with digital filter
- Hi-to-Lo, Lo-to-Hi latch

Each digital input channel can set its operational mode independently.

Digital Output

The ADAM-6050 & ADAM-6051 digital output channels also provide four operational modes: normal digital output, pulse output with continuous or burst count mode, Hi-to-Lo, Lo-to-Hi delay. Each digital output channel can set its operational mode independently as well.

Counter/Frequency

The ADAM-6051 offers two 32-bit counter channels and a built-in programmable timer for frequency measurement.

Programmable Alarm Output

The ADAM-6051 modules include two digital output channels for alarm functions. You can set alarm values (32-bit) into the module from your host computer.

Relay Output Module

The ADAM-6060 offers six isolated digital input channels and six isolated relay channels. The digital input channel accepts 10 ~ 30 V_{DC} input. Just like other ADAM modules, the ADAM-6060 relay module is controlled remotely and stores its configuration data in EEPROM. It provides six Form A relay channels with 24 V_{AC} output. This module is excellent for on/off control or low-power switching applications.

12-ch Universal Input/Output Module

The ADAM-6024 offers six analog inputs, two analog outputs, two digital inputs and two digital outputs. This module is especially cost-effective for applications that require various signal type I/O points. The ADAM-6000 series also offers analog output functions.

Appendix E

CR1000 datalogger, specifications

Section 6. CR1000 Specifications

CR1000 specifications are valid from –25° to 50°C in non-condensing environments unless otherwise specified. Recalibration is recommended every two years. Critical specifications and system configurations should be confirmed with a Campbell Scientific applications engineer before purchase.

PROGRAM EXECUTION RATE
10 ms to one day at 10 ms increments

ANALOG INPUTS (SE 1–16, DIFF 1–8)
Eight differential (DIFF) or 16 single-ended (SE) individually configured input channels. Channel expansion provided by optional analog multiplexers.
RANGES and RESOLUTION: With reference to the following table, basic resolution (Basic Res) is the resolution of a single *A/D* *(p. 447)* conversion. A DIFF measurement with input reversal has better (finer) resolution by twice than Basic Res.

Range (mV)[1]	DIFF Res (µV)[2]	Basic Res (µV)
±5000	667	1333
±2500	333	667
±250	33.3	66.7
±25	3.33	6.7
±7.5	1.0	2.0
±2.5	0.33	0.67

[1]Range overhead of ≈9% on all ranges guarantees full-scale voltage will not cause over-range.
[2]Resolution of DIFF measurements with input reversal.

ANALOG INPUT ACCURACY[3]:
±(0.06% of reading + offset[3]), 0° to 40°C
±(0.12% of reading + offset[3]), -25° to 50°C
±(0.18% of reading + offset[3]), -55° to 85°C (-XT only)
[3]Accuracy does not include sensor and measurement noise. Offset definitions:
Offset = 1.5 x Basic Res + 1.0 µV (for DIFF measurement w/ input reversal)
Offset = 3 x Basic Res + 2.0 µV (for DIFF measurement w/o input reversal)
Offset = 3 x Basic Res + 3.0 µV (for SE measurement)
ANALOG MEASUREMENT SPEED:

Inte-gration Type Code	Inte-gration Time	Settling Time	---Total Time[4]--- SE with no Rev	DIFF with Input Rev
250	250 µs	450 µs	≈1 ms	≈12 ms
_60Hz[5]	16.67 ms	3 ms	≈20 ms	≈40 ms
_50Hz[5]	20.00 ms	3 ms	≈25 ms	≈50 ms

[4]Includes 250 µs for conversion to engineering units.
[5]AC line noise filter

INPUT-NOISE VOLTAGE: For DIFF measurements with input reversal on ±2.5 mV input range (digital resolution dominates for higher ranges):
250 µs Integration: 0.34 µV RMS
50/60 Hz Integration: 0.19 µV RMS
INPUT LIMITS: ±5 Vdc
DC COMMON-MODE REJECTION: >100 dB
NORMAL-MODE REJECTION: 70 dB @ 60 Hz when using 60 Hz rejection
INPUT VOLTAGE RANGE W/O MEASUREMENT CORRUPTION: ±8.6 Vdc max.
SUSTAINED-INPUT VOLTAGE W/O DAMAGE: ±16 Vdc max.
INPUT CURRENT: ±1 nA typical, ±6 nA max. @ 50°C; ±90 nA @ 85°C
INPUT RESISTANCE: 20 GΩ typical
ACCURACY OF BUILT-IN REFERENCE JUNCTION THERMISTOR (for thermocouple measurements):
±0.3°C, -25° to 50°C
±0.8°C, -55° to 85°C (-XT only)

ANALOG OUTPUTS (VX 1–3)
Three switched voltage outputs sequentially active only during measurement.
RANGES AND RESOLUTION:

Channel	Range	Resolu-tion	Current Source / Sink
(VX 1–3)	±2.5 Vdc	0.67 mV	±25 mA

ANALOG OUTPUT ACCURACY (VX):
±(0.06% of setting + 0.8 mV, 0° to 40°C
±(0.12% of setting + 0.8 mV, -25° to 50°C
±(0.18% of setting + 0.8 mV, -55° to 85°C (-XT only)
VX FREQUENCY SWEEP FUNCTION: Switched outputs provide a programmable swept frequency, 0 to 2500 mV square waves for exciting vibrating wire transducers.

PERIOD AVERAGE
Any of the 16 SE analog inputs can be used for period averaging. Accuracy is ±(0.01% of reading + resolution), where resolution is 136 ns divided by the specified number of cycles to be measured.
INPUT AMPLITUDE AND FREQUENCY:

Volt-age Gain	Range Code	Input Signal Peak-Peak Min mV[6]	Max V[7]	Min Pulse Width µs	Max Freq kHz[8]
1	mV250	500	10	2.5	200
10	mV25	10	2	10	50
33	mV7_5	5	2	62	8
100	mV2_5	2	2	100	5

[6]Signal to be centered around *Threshold* (see **PeriodAvg()** instruction).
[7]Signal to be centered around ground.
[8]The maximum frequency = 1/(twice minimum pulse width) for 50% of duty cycle signals.

RATIOMETRIC MEASUREMENTS
MEASUREMENT TYPES: The CR1000 provides ratiometric resistance measurements using voltage excitation. Three switched voltage excitation outputs are available for measurement of four- and six-wire full bridges, and two-, three-, and four-wire half bridges. Optional excitation polarity reversal minimizes dc errors.
RATIOMETRIC MEASUREMENT ACCURACY[9,11]
Note Important assumptions outlined in footnote 9:
±(0.04% of Voltage Measurement + Offset[12])
[9]Accuracy specification assumes excitation reversal for excitation voltages < 1000 mV. Assumption does not include bridge resistor errors and sensor and measurement noise.
[11]Estimated accuracy, ΔX (where X is value returned from measurement with **Multiplier** =1, **Offset** = 0):
BRHalf() Instruction: $\Delta X = \Delta V_1 / V_X$.
BRFull() Instruction: $\Delta X = 1000 \times \Delta V_1 / V_X$, expressed as $mV \bullet V^{-1}$.
Note ΔV_1 is calculated from the ratiometric measurement accuracy. See manual section *Resistance Measurements* *(p. 295)* for more information.
[12]Offset definitions:
Offset = 1.5 x Basic Res + 1.0 µV (for DIFF measurement w/ input reversal)
Offset = 3 x Basic Res + 2.0 µV (for DIFF measurement w/o input reversal)
Offset = 3 x Basic Res + 3.0 µV (for SE measurement)
Note Excitation reversal reduces offsets by a factor of two.

PULSE COUNTERS (P 1–2)
Two inputs individually selectable for switch closure, high frequency pulse, or low-level ac. Independent 24-bit counters for each input.
MAXIMUM COUNTS PER SCAN: 16.7 x 10^6
SWITCH-CLOSURE MODE:
Minimum Switch Closed Time: 5 ms
Minimum Switch Open Time: 6 ms
Max. Bounce Time: 1 ms open without being counted
HIGH-FREQUENCY PULSE MODE:
Maximum-Input Frequency: 250 kHz
Maximum-Input Voltage: ±20 V
Voltage Thresholds: Count upon transition from below 0.9 V to above 2.2 V after input filter with 1.2 µs time constant.
LOW-LEVEL AC MODE: Internal ac coupling removes dc offsets up to ±0.5 Vdc.
Input Hysteresis: 12 mV RMS @ 1 Hz
Maximum ac-Input Voltage: ±20 V
Minimum ac-Input Voltage:

Sine wave (mV RMS)	Range (Hz)
20	1.0 to 20
200	0.5 to 200
2000	0.3 to 10,000
5000	0.3 to 20,000

DIGITAL I/O PORTS (C 1-8)
Eight ports software selectable as binary inputs or control outputs. Provide on/off, pulse width modulation, edge timing, subroutine interrupts / wake up, switch-closure pulse counting, high-frequency pulse counting, asynchronous communications (UARTs), and SDI-12 communications. SDM communications are also supported.

DIGITAL I/O PORTS (C 1-8)
Eight ports software selectable as binary inputs or control outputs. Provide on/off, pulse width modulation, edge timing, subroutine interrupts / wake up, switch-closure pulse counting, high-frequency pulse counting, asynchronous communications (UARTs), and SDI-12 communications. SDM communications are also supported.
LOW FREQUENCY MODE MAX: <1 kHz
HIGH FREQUENCY MODE MAX: 400 kHz
SWITCH-CLOSURE FREQUENCY MAX: 150 Hz
EDGE-TIMING RESOLUTION:
OUTPUT VOLTAGES (no load): high 5.0 V ±0.1 V; low < 0.1 V
OUTPUT RESISTANCE: 330 Ω
INPUT STATE: high 3.8 to 16 V; low -8.0 to 1.2 V
INPUT HYSTERISIS: 1.4 V
INPUT RESISTANCE:
100 kΩ with inputs < 6.2 Vdc
220 Ω with inputs ≥ 6.2 Vdc
SERIAL DEVICE / RS-232 SUPPORT: 0 to 5 Vdc UART

SWITCHED 12 Vdc (SW-12)
One independent 12 Vdc unregulated terminal switched on and off under program control. Thermal fuse hold current = 900 mA at 20°C, 650 mA at 50°C, and 360 mA at 85°C.

CE COMPLIANCE
STANDARD(S) TO WHICH CONFORMITY IS DECLARED:
IEC61326:2002

COMMUNICATION
RS-232 PORTS:
DCE nine-pin: (not electrically isolated) for computer connection or connection of modems not manufactured by Campbell Scientific.
COM1 to COM4: four independent Tx/Rx pairs on control ports (non-isolated); 0 to 5 Vdc UART
Baud Rate: selectable from 300 bps to 115.2 kbps.
Default Format: eight data bits; one stop bits; no parity.
Optional Formats: seven data bits; two stop bits; odd, even parity.
CS I/O PORT: Interface with telecommunications peripherals manufactured by Campbell Scientific.
SDI-12: Digital control ports C1, C3, C5, C7 are individually configurable and meet SDI-12 Standard v. 1.3 for datalogger mode. Up to ten SDI-12 sensors are supported per port.
PERIPHERAL PORT: 40-pin interface for attaching CompactFlash or Ethernet peripherals.
PROTOCOLS SUPPORTED: PakBus, AES-128 Encrypted PakBus, Modbus, DNP3, FTP, HTTP, XML, HTML, POP3, SMTP, Telnet, NTCIP, NTP, Web API, SDI-12, SDM.

SYSTEM
PROCESSOR: Renesas H8S 2322 (16-bit CPU with 32-bit internal core running at 7.3 MHz)
MEMORY: 2 MB of flash for operating system; 4 MB of battery-backed SRAM for CPU usage, program storage, and final data storage.
REAL-TIME CLOCK ACCURACY: ±3 min. per year. Correction via GPS optional.
RTC CLOCK RESOLUTION: 10 ms

SYSTEM POWER REQUIREMENTS
VOLTAGE: 9.6 to 16 Vdc
INTERNAL BATTERY: 1200 mAhr lithium battery for clock and SRAM backup. Typically provides three years of back-up.
EXTERNAL BATTERIES: Optional 12 Vdc nominal alkaline and rechargeable available. Power connection is reverse polarity protected.
TYPICAL CURRENT DRAIN at 12 Vdc:
Sleep Mode: 0.7 mA typical; 0.9 mA maximum
1 Hz Sample Rate (one fast SE meas.) mA
100 Hz Sample Rate (one fast SE meas.): 16 mA
100 Hz Sample Rate (one fast SE meas. with RS-232 communications): 28 mA
Active external keyboard display adds 7 mA (100 mA with backlight on).

PHYSICAL
DIMENSIONS: 239 x 102 x 61 mm (9.4 x 4.0 x 2.4 in.) ; additional clearance required for cables and leads.
MASS / WEIGHT: 1.0 kg / 2.1 lbs

WARRANTY
Warranty is stated in the published price list and in opening pages of this and other user manuals.

Appendix F

Clinotronic PLUS, specifications

WYLER AG
Im Hölderli
CH-8405 WINTERTHUR
Switzerland

Tel. 0041 (0) 52 233 66 66
Fax. 0041 (0) 52 233 20 53

Homepage: http://www.wylerag.com
E-Mail: wyler@wylerag.com

OPERATOR'S MANUAL

Clinotronic PLUS

The intelligent universal inclinometer

File: „clino_e.doc“

4. TECHNICAL SPECIFICATIONS

4.1. GENERAL

Measuring range Messbereich		**± 10 Arcdeg**	**± 30 Arcdeg**	**± 45 Arcdeg**
Calibration / Kalibrierung	Last values at: / letzte Werte bei:	± 10 Arcdeg	± 30 Arcdeg	± 50 Arcdeg resp. ± 60 Arc.deg.
Limits of Error / Fehlergrenze		< 1 Arcmin + 1 Digit	< 1.5 Arcmin + 1 Digit	< 2 Arcmin + 1 Digit
Settle time / Messzeit	Value available after / Anzeige nach:	< 2 Secs.		
Resolution / Auflösung	Dep. on units set / abhängig von Einstellung	> 5 Arcsec (0.025 mm/m)		
Temp. Coeff. / Temperatur-Koeff.	Zero and scale / Null und Skala	< 0.01 Arcdeg./°C		
Data connection / Anschluss		RS485 / asynchron / 7 Bit / 2 Stop Bit / no parity / 9600 Baud		
Battery / Batterie		1 x Size AA 1.5V Alkaline		
Battery life / Betriebsdauer	In full operation / Vollbetrieb	Size AA 1.5V Alkaline / 25 hrs		
Housing / Gehäuse	Aluminium hard anodised	100 x 75 x 30 mm		
Weight / Gewicht		400 g, incl. Battery		
Temp. range / Temp. -Bereich	Operating Storage	0 to 40 °C. -20 to 70 °C.		
CE conformity	Emission: Immunity:	fulfilled: fulfilled:	EN61000-6-3 EN61000-6-2	

4.2 SPECIFICATIONS FOR PORT CONNECTION

4.2.1. DATA TRANSFER: Asynchron / 7 Data Bit / 2 Stop Bit / No Parity / 9600 Baud

4.2.2. PIN DEFINITION / CONNECTOR

Connector: 8pol Binder Series 712 female

PIN-definition:

- 1
- 2 GND
- 3 +5V
- 4 RTA
- 5 RTB
- 6
- 7 RTS
- 8

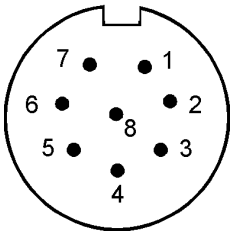

Outside view of connector

Remarks: Additional information concerning data transfer see APPENDIX A